Finite Fracture Mechanics at the micro-scale. Application to bending tests of micro cantilever beams

Sara Jiménez Alfaro, Dominique Leguillon

Finite Fracture Mechanics at the micro-scale. Application to bending tests of micro cantilever beams

Sara Jiménez Alfaro*, Dominique Leguillon

Institut Jean Le Rond d'Alembert
Sorbonne Université – CNRS UMR 7190
4 place Jussieu, 75000, PARIS, France

* Corresponding author: sara.jimenez@sorbonne-universite.fr

Abstract: In the framework of Finite Fracture Mechanics theory, the Coupled Criterion predicts crack onset based, totally or partially according to the situation, on an energy condition. Due to the smallness of the specimens at the micro-scale, this condition may become difficult to be satisfied given the very small volume of the structures, leading to an apparent strengthening. The aim of this work is to analyze how the answer brought by the Coupled Criterion evolves when descending the scales from the cm-scale, to the µm-scale and even nm-scale. It is based on case studies and on comparisons with experiments found in the literature. Obviously, the Coupled Criterion still works at the micro-scale. However, due to the lack of energy caused by the smallness of the specimens, it is in general much sensitive to the toughness whereas it is little sensitive to the tensile strength, making it sometimes difficult to identify this latter parameter. In parallel, the difference between displacement and force controlled loading modes increases when descending the scales and a notch insensitivity appears.

Nomenclature

a	Notch depth
A, A^*	Scaling coefficients involved in the Coupled Criterion
d	Notch width
E	Young's modulus
F	Applied force
F_c	Critical applied force at failure
F_i^{exp}	Measured applied force on specimen i
F_i^{sim}	Predicted applied force on specimen i using the coupled criterion
G	Energy release rate
G_c	Fracture energy
$\tilde{G}_c$	Predicted fracture energy from the minimization process
$\overline{G}_c$	Averaged fracture energy from the $\tilde{G}_{ic}$
$\tilde{G}_{ic}$	Predicted fracture energy for specimen i
G_{inc}	Incremental energy release rate
k	Generalized stress intensity factor
k_c	Critical value of the generalized stress intensity factor

K_{Ic}	Material toughness
l	Crack length
L	Specimen length
L_{c}	Critical specimen length
l_{Irwin}	Irwin's length
$\underline{u}$	Eigenfunction associated to λ in Williams' expansion
$\underline{U}$	Elastic displacement field
U_{d}	Prescribed displacement at failure
r, θ	Polar coordinates
t	Specimen thickness
W	Specimen width
x_1, x_2	Cartesian coordinates
δl	Newly created crack length according to the CC (general approach)
δl_{c}	Newly created crack length according to the CC (asymptotic approach)
δS	Newly created crack surface
λ	Singularity exponent
ν	Poisson's ratio
ρ	Notch root radius
σ	Tensile component of the stress tensor
σ_{f}	Equivalent flexural strength
σ_{c}	Tensile strength
$\tilde{\sigma}_{\mathrm{c}}$	Predicted tensile strength from the minimization process
$\bar{\sigma}_{\mathrm{c}}$	Averaged tensile strength from the $\tilde{\sigma}_{ic}$
$\tilde{\sigma}_{ic}$	Predicted tensile strength for specimen *i*
ω	Notch opening angle
Π_{k}	Kinetic energy
Π_{p}	Potential energy
CC	Coupled criterion
DC	Displacement Controlled
FC	Force Controlled
GSIF	Generalized Stress Intensity Factor
SIF	Stress Intensity Factor
ERR	Energy Release Rate
FE	Finite Element
FFE	Full Finite Element
FFM	Finite Fracture Mechanics
FIB	Focused Ion Beam
IERR	Incremental Energy Release Rate
MAE	Matched Asymptotic Expansions
MD	Molecular dynamics
MEMS	Micro-Electro-Mechanical System
PF	Phase field
SPM	Scanning Probe Microscopy

1. Introduction

Advances in micro-technology over the past century have highlighted the need for studies to understand the mechanical behaviour of materials at the micro-scale. Among the latest developments are the evolution of the microelectronics industry, with the manufacture of small size components [1], such as inter-layer dielectric and chip passivation films [2]. Furthermore, the nuclear industry is also in demand for a better knowledge of the behaviour of fuels such as UO_2 in pressurized water reactors [5,6]. It is also important to highlight the tendency to mimic natural materials like mother-of-pearl to create nacre-like inorganic materials [7,8].

Experimental tests at small scales can be made following two routes. On the one hand, using diminished test rigs in which very small displacements or forces are applied. These techniques evolved significantly in the 80's with the beginning of new technologies for small-scale experimentation. According to [3], two types of micro-scale testing appeared at that time: SPM (Scanning Probe Microscopy) techniques, which started with the invention of the STM (Scanning Tunneling Microscopy) [9] and nano-indentation [10]. The latter was firstly used on surfaces in bulk materials or coatings. On the other hand, MEMS (Micro-Electro-Mechanical System) technology can be used to fabricate, using lithography techniques, structures in which the sensors, the specimen and sometimes the actuator are all integrated [3]. These structures are called *lab on chip*. According to [citaEspinosa], Kahn et al. [citaKahn2000] and Ballarini et al [citaBallarini1997] were pioneers on the fracture mechanical analysis with sharp cracks. Both performed the tests on polysilicon MEMS devices, using indentation to generate pre-existing defects on the specimens. Another example considering MEMS technology can be found in [4]. Furthermore, the FIB (Focused Ion Beam) [11] technique is used to fabricate micro-specimens of ceramic materials. Since the application of this technology on micro-compression testing by Uchic et al. [cita Uchic], it has been deeply applied in many studies, e.g. bending of notched and chevron notched micro-cantilever beams in [12-14], and compression on micro-pillars in [3,15].

Most of the above references are concerned to fracture properties. Then, the question that arises is: can fracture mechanics theories be extended to small scales? In this paper we focus on Finite Fracture Mechanics (FFM) [16-19] and more precisely on the Coupled Criterion (CC) [18,19] which have been successfully used to predict the crack onset at the macro-scale. Attempts to use the CC at the micro-scale have been made [1,5] and have brought into evidence how important a good knowledge of the fracture parameters (strength and fracture energy or toughness) is at this scale.

The main objective of this paper is to verify the applicability of the CC at the micro-scale through case studies and comparisons to experiments. In particular, it discuss the reliability of experiments made at the micro- and nano-scale to obtain fracture properties, since an apparent strengthening of the material due to its smallness is observed, disregarding any statistical consideration on the presence and size of defects.

It is outlined as follows. Section 2 proposes some reminders on the CC and on the two approaches that can be used to predict crack onset: Match Asymptotic Expansions (MAE) and Full Finite Element (FFE) computations. Section 3 is dedicated to case studies. It starts by a preliminary remark in which a bar in tension is analysed to bring into evidence the differences in interpretation of the CC depending on the scale and raises questions about the tensile strength parameter. Then, three-point bending tests on V-notched, U-notched and unnotched specimens are analyzed at different scales, enlightening the different influences of the fracture energy and the tensile strength parameters according to the scale. They also show that there is an increasing difference between force and displacement controlled loading modes when descending the scales. Finally, in Section 4, comparisons with experiments found in the literature are carried

out. They highlight again the need but also the difficulty to identify the parameters of rupture and especially the tensile strength.

2. The Coupled Criterion

The CC allows predicting crack nucleation in brittle materials. It has been successfully applied in several problems at the macro-scale, such as notched specimens, laminates, adhesive joints or embedded inclusions [19]. This criterion is corroborated by previous experiments on transverse cracking in cross-ply laminates [20].
According to the CC, two necessary conditions are together sufficient to predict the crack nucleation, since fracture occurs when both are simultaneously fulfilled: (i) an energy condition, based on an energy balance, and (ii) a stress condition.

(i) The energy balance is obtained considering two states of the loaded structure, prior to and following a crack onset. The potential and kinetic energy related to each state is characterized by $\Pi_{\mathrm{p}}^{(i)}$ and $\Pi_{\mathrm{k}}^{(i)}$, where the superscript $i = 0,1$ is related to the state we are referring to. The initial one, $i = 0$, elasto-static, is characterized by a potential energy $\Pi_{\mathrm{p}}^{(0)}$ and a zero kinetic energy $\Pi_{\mathrm{k}}^{(0)} = 0$, whereas the final state, $i = 1$, is defined after the onset of a new crack or the growth of a preexisting one. Hence, we have

$$\Pi_{\mathrm{p}}^{(0)} = \Pi_{\mathrm{p}}^{(1)} + \Pi_{\mathrm{k}}^{(1)} + G_{\mathrm{c}}\delta S \tag{1}$$

where $\Pi_{\mathrm{p}}^{(1)}$ and $\Pi_{\mathrm{k}}^{(1)}$ are the potential and kinetic energy related to the final state, respectively, G_{c} is the fracture energy per unit surface, and δS is the newly created crack surface. Both the final potential and kinetic energy can be defined as $\Pi_{\mathrm{p}}^{(1)} = \Pi_{\mathrm{p}}^{(0)} + \delta\Pi_{\mathrm{p}}$ and $\Pi_{\mathrm{k}}^{(1)} = \delta\Pi_{\mathrm{k}}$. Therefore,

$$\delta\Pi_{\mathrm{p}} + \delta\Pi_{\mathrm{k}} + G_{\mathrm{c}}\delta S = 0 \tag{2}$$

Since $\delta\Pi_{\mathrm{k}} \geq 0$, we have

$$\delta\Pi_{\mathrm{p}} + G_{\mathrm{c}}\delta S \leq 0 \tag{3}$$

which is the necessary energy condition for crack nucleation since it derives from the unquestionable energy balance (1).
In the following, equations will be defined in the 2D domain. It means that the condition can be rewritten considering the newly created crack length δl

$$\delta\Pi_{\mathrm{p}} + G_{\mathrm{c}}\delta l \leq 0 \tag{4}$$

Being understood that $\delta\Pi_{\mathrm{p}}$ is now defined per unit thickness of the specimen. This is commonly written, introducing the Incremental Energy Release Rate (IERR) [18], as

$$-\frac{\delta\Pi_{\mathrm{p}}}{\delta l} = G_{\mathrm{inc}}(\delta l) \geq G_{\mathrm{c}} \tag{5}$$

In this relationship, δl is unknown. Griffith (1921) considered the limit as $\delta l \to 0$

$$-\frac{\partial\Pi_{\mathrm{p}}}{\partial l} = G \geq G_{\mathrm{c}} \tag{6}$$

where G is the Energy Release Rate (ERR). However, it is well-known that if there is no pre-existing crack $G = 0$, hence, the onset of a crack at a stress concentration point which is not a crack tip cannot be predicted using (6).

(ii) On the other hand, the stress condition is based on a maximum tension that a material can undergo, known as the tensile strength σ_{c}. According to the CC, the tensile stress in the initial state must be higher than the tensile strength all along the presupposed crack path to allow crack onset

$$\sigma(x_2) \geq \sigma_{\mathrm{c}} \quad \text{for} \quad 0 \leq x_2 \leq \delta l \tag{7}$$

where x_2 is the coordinate along the expected crack path. As a consequence of the two inequalities (5) and (7), it can be shown that the crack nucleation occurs abruptly from 0 to a length δl. It is important to highlight that this incremental form is the foundation of FFM, since it assumes the instantaneous formation of cracks of finite size [16-19]. Moreover, in the case of the CC this instantaneous crack onset is not an assumption but the consequence of the two inequalities (6) and (7) as shown in [18].
To sum up, the crack nucleation is predicted by the CC using two necessary and together sufficient conditions

$$\frac{G_{\mathrm{inc}}(\delta l)}{G_{\mathrm{c}}} \geq 1 \tag{8}$$

$$\frac{\sigma(x_2)}{\sigma_{\mathrm{c}}} \geq 1 \quad \text{for} \quad 0 \leq x_2 \leq \delta l \tag{9}$$

Note that, in general, $\sigma(x_2)$ is a decreasing function of x_2 and the second inequality reduces to

$$\frac{\sigma(\delta l)}{\sigma_{\mathrm{c}}} \geq 1 \tag{10}$$

Remark: In this approach, the exact amount of kinetic energy that can be produced during the initiation process is ignored. It is simply considered as positive (see eqns. (2) and (3)). Its influence on the CC was studied by Laschuetza et al. [21] who explained that the load at initiation is well captured by the CC (at least in the case they study), only the transient process following initiation is not described by the CC. Moreover, in the micro-scale cases studied further (Section 4.1), the kinetic energy remains likely very small. Otherwise, it would seem

difficult to perform tests under force-controlled loading, since most indenters do not allow the control of displacements [3].

2.1. *Asymptotic approach*

The MAE procedure, is a quasi-analytical formulation that allows to describe the crack nucleation at the tip of sharp V-notches under the assumption that the crack nucleation length δl is small compared to any dimension of the structure (often the notch depth as a reference). It is based on Williams' expansion [21] of the displacements field $\underline{U}(x_1, x_2)$ in the neighborhood of the singularity generated by a reentrant corner

$$\underline{U}(x_1, x_2) = \underline{U}(0,0) + kr^{\lambda}\underline{u}(\theta) + ... \tag{11}$$

where $\underline{U}(0,0)$ is the rigid displacement of the origin set at the tip of the notch, x_1, x_2 are the Cartesian coordinates and r, θ the polar ones. The parameter k is the Generalized Stress Intensity Factor (GSIF) of the singular term defined by the exponent of the singularity λ and the associated shape function $\underline{u}(\theta)$. The scalar λ and the function $\underline{u}(\theta)$ form the pair eigenvalue-eigenfunction of a specific problem [22].
Then, the IERR (see (5)), as well as the tensile stress at a distance δl can be expanded as (E is the Young modulus and ν the Poisson ratio)

$$\begin{aligned} &G_{\text{inc}}(\delta l) = Ak^2\delta l^{2\lambda-1} + ... \text{ with } A = \frac{(1-\nu^2)A^*}{E} \\ &\sigma(\delta l) = k\delta l^{\lambda-1} + ... \end{aligned} \tag{12}$$

with an appropriate normalization of $\underline{u}(\theta)$. In (12), A^* is a dimensionless scaling coefficient depending on the opening angle ω (Figure 3). The coefficient $1-\nu^2$ relies on the plane strain assumption used throughout this paper. Following [18], the energy condition provides a lower bound for admissible crack extension lengths δl while the stress condition gives an upper bound. Then, using the Irwin length l_{Irwin} [23], compatibility between the two conditions provides the crack initiation length δl_{c}

$$\delta l_{\text{c}} = \frac{l_{\text{Irwin}}}{A^*} \text{ with } l_{\text{Irwin}} = \frac{EG_{\text{c}}}{(1-\nu^2)\sigma_{\text{c}}^2} \tag{13}$$

To ensure the validity of the asymptotic expansions, its smallness is checked afterward.
Finally, the CC takes the following form, involving the critical value k_{c} of the GSIF k

$$k \geq k_{\text{c}} = \left(\frac{EG_{\text{c}}}{(1-\nu^2)A^*}\right)^{1-\lambda} \sigma_{\text{c}}^{2\lambda-1} \tag{14}$$

This holds true disregarding the way of loading.

Table 1 reports the length at initiation δl_c and the critical GSIF k_c for various opening angles (material data are for alumina-zirconia ceramic as given in Section 3.1). Note that no length is given for a crack ($\omega = 0$ deg.), since Griffith's criterion [24] (with which the CC coincides for a crack) does not involve any length. Indeed, observe that $2\lambda - 1 = 0$ in (12) so that no lower bound exists for admissible crack extension lengths. Thus, any infinitely small extension can be considered which justifies the use of the derivative in (6) in case of preexisting crack.

Table 1. CC parameters extracted from the asymptotic approach. Let us recall that for a crack ($\omega = 0$ deg.) $k_c = K_{Ic} = 38.23$ MPa mm$^{1/2}$ (derived from G_c using Irwin's formula) and for a straight edge ($\omega =$ 180 deg.) $k_c = \sigma_c =$ 400 MPa.

ω (deg.)	0	30	60	90	120	150
λ	0.500	0.502	0.512	0.545	0.616	0.752
A^*	6.28	6.16	5.82	5.18	4.25	3.03
δl_c (μm)		9.3	9.7	11.1	13.5	18.9
k_c (MPa mm$^{1-\lambda}$)	38.23	38.98	41.99	51.57	76.59	149.58

2.4 *Full Finite Element approach*

In some cases the assumption of smallness of δl_c may not be verified, the Full Finite Element (FFE) approach [25] gets rid of this limitation. The whole structure under consideration is modelled by FE either under a prescribed displacement or a prescribed force. In a first step an undamaged configuration is considered, i.e. with no new crack in the structure. The tensile stress $\sigma(x_2)$ along the expected crack path is computed together with the potential energy $\Pi_p(0)$. Then, nodes along the crack path are released one after the other, generating a virtual crack with increasing length δl and allowing the computation of $\Pi_p(\delta l)$ and then $G_{inc}(\delta l)$. Notice that several calculations are required to build the function $G^{inc}(\delta l)$ in the FFE approach. Obviously, the computational cost is higher than in the MAE approach. But, of course, this procedure is valid without restrictions, whereas the MAE approach needs a smallness assumption. In any case, whatever the approach, the numerical effort remains small compared to other approaches involving the resolution of non-linear problems like cohesive zone models [26] or phase field method [27,28].

Different cases that could be met when implementing the CC are illustrated in Figure 1 and refer to coming examples. The load is gradually increased so that a first point fulfilling the two conditions of the CC appears (black arrow). Figure 1a is the classically encountered situation where σ / σ_c is a decreasing function while G_{inc} / G_c is monotonically increasing. In Figure 1b, σ / σ_c is still decreasing but G_{inc} / G_c is no longer monotonically increasing, it goes through a maximum and then decreases. On the contrary, in Figure 1c, it is σ / σ_c which is no longer monotonically decreasing while G_{inc} / G_c is increasing. These situations were already discussed in [30,31].

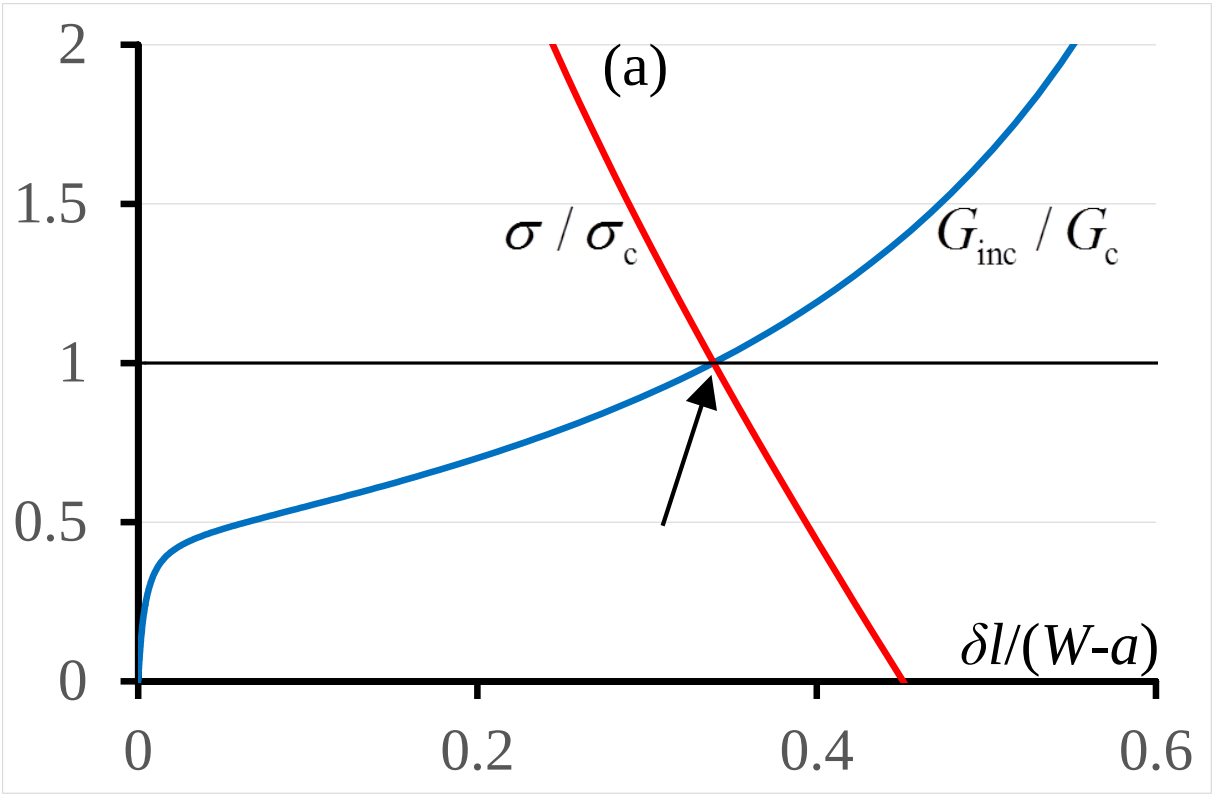
(a)
2
1.5
1
0.5
0
0
0.2
0.4
0.6
σ / σc
Ginc / Gc
δl/(W-a)

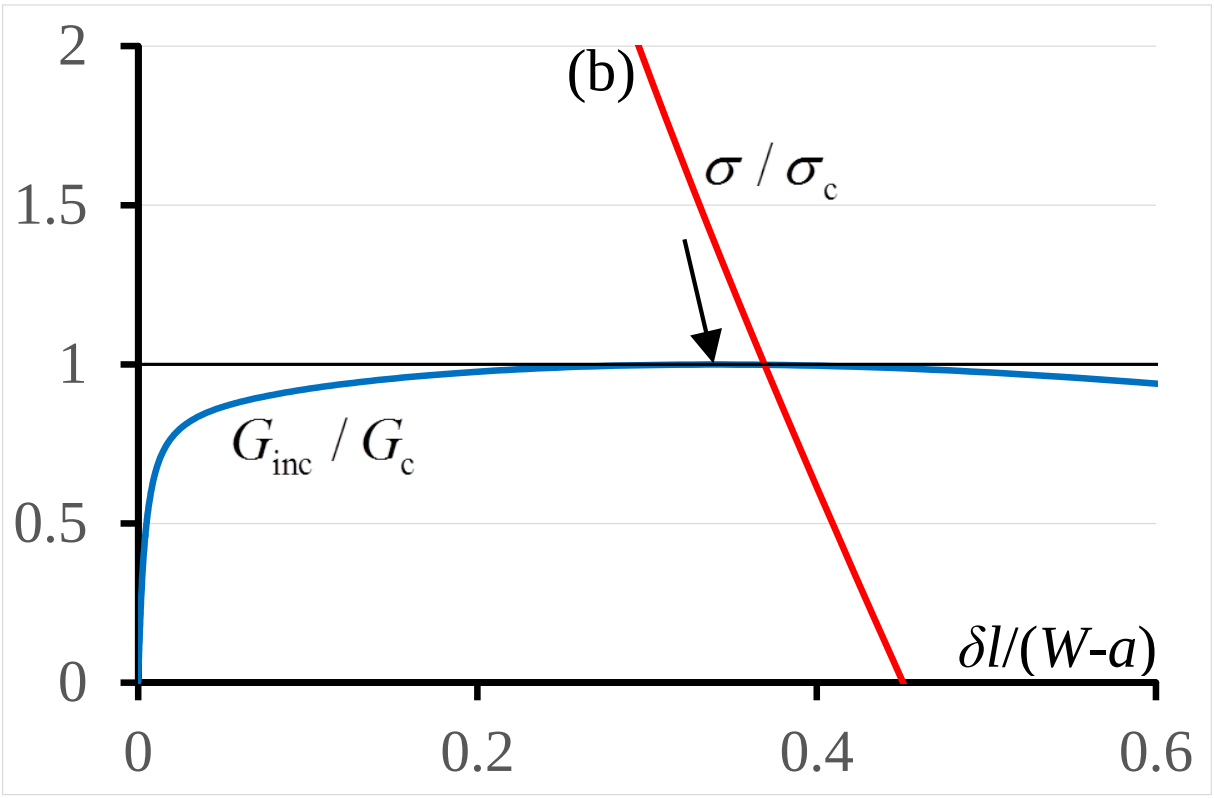
(b)
2
1.5
1
0.5
0
0
0.2
0.4
0.6
σ / σc
Ginc / Gc
δl/(W-a)

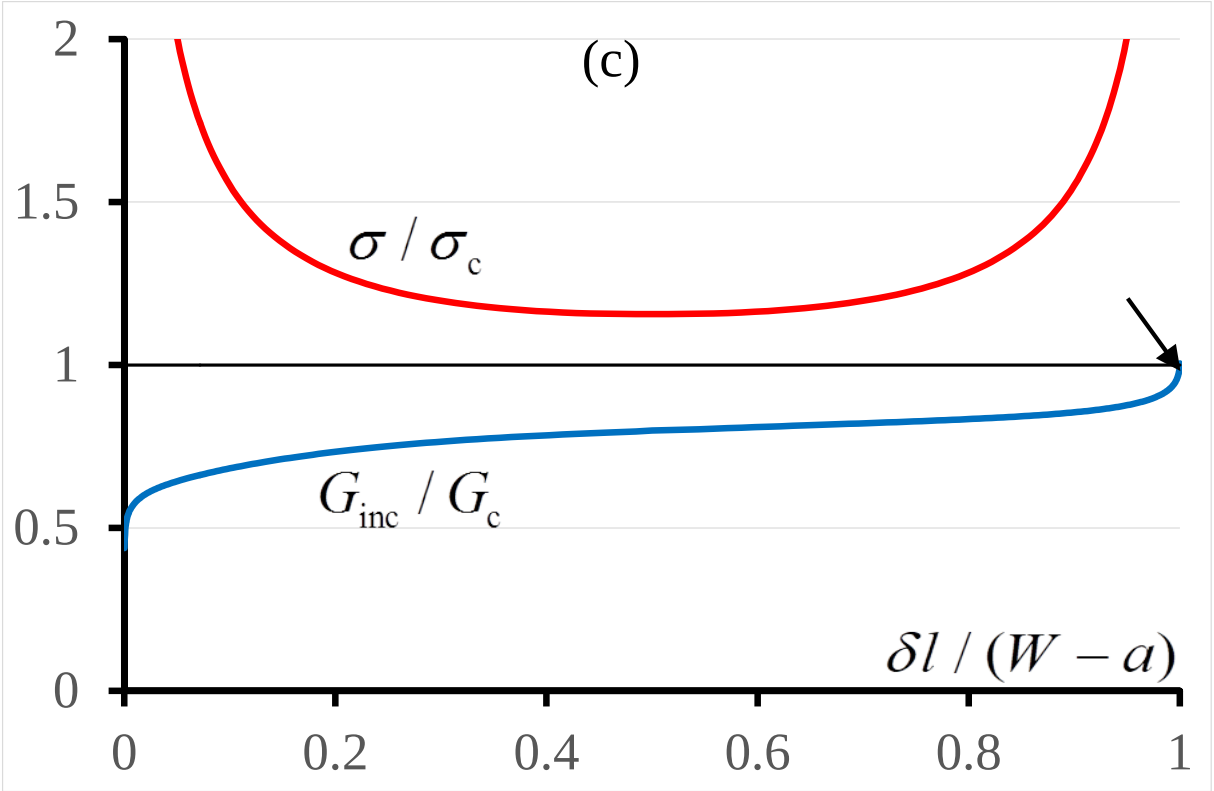

Figure 1. Examples of implementation of the CC. (a) The U-notched specimen at the µ-scale under FC loading (Section 3.5). (b) The U-notched specimen at the µ-scale under DC loading (Section 3.5). (c) The double edge notched specimen at the nm-scale under DC loading (Section 4.3). Stress condition (10): red solid line, energy condition (8): blue solid line. The horizontal axis is the crack length normalized by the ligament width. The arrow shows the point that meets the two conditions. Refer to Section 3 for DC and FC meaning.

3. Case studies

The purpose of this section is to highlight the differences in interpretation of the CC depending on the scale at which the simulations are conducted, it is based on case studies. Comparisons with experiments taken from the literature will be made in the next section.

3.1 *A preliminary remark*

An elastic bar in tension with length L and cross-section surface S is submitted to a tensile force F (Figure 2).

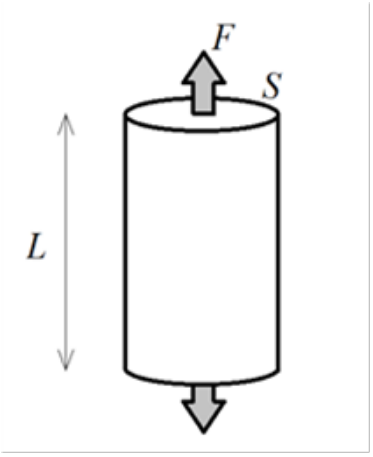

Figure 2. A bar in tension.

Since there is no longer any potential energy once the bar is broken, the change in potential energy Π_p between the unbroken and the broken state is

$$\Pi_p(0) - \Pi_p(S) = \frac{1}{2}\frac{\sigma^2}{E} LS \tag{15}$$

where $\sigma = F / S$. The energy dissipated during failure is $G_c S$ and the energy condition gives

$$\frac{1}{2}\frac{\sigma^2}{E} LS \geq G_c S \;\Rightarrow\; \sigma \geq \sqrt{\frac{2EG_c}{L}} \tag{16}$$

According to the CC, the stress condition (7) must be added and clearly governs provided L is large enough, i.e. larger than L_c

$$L > L_c = \frac{2EG_c}{\sigma_c^2} \tag{17}$$

Then, under a monotonic loading, failure occurs for $F = F_c = \sigma_c S$.

But if L is smaller than the critical value L_c, it is now the energy condition that takes precedence and failure occurs at a load such that $\sigma > \sigma_c$, which may be erroneously interpreted as a strengthening effect in short bars while it is a size effect only due to a lack of energy. Note that the surface of the cross-section plays no role, while the length does.

For an alumina-zirconia ceramic, Young's modulus, Poisson's ratio, tensile strength and fracture energy are reported in [29] to be: E = 380 GPa, ν = 0.22, σ_c = 400 MPa, G_c = 0.023 MPa mm (23 J m^{-2}). It gives L_c = 109 µm, thus, a 10 µm long bar will break in tension for σ = 1322 MPa which should not be confused with the tensile strength set here at 400 MPa. Note that this result would remain unchanged as long as $\sigma_c \leq 1322$ MPa.

Obviously, this kind of experiment seems poorly appropriate to determine a tensile strength (by the way, Dehm et al. [3] use the word "strength" in quotation marks). This reasoning is also valid for compression tests on micro-pillars [3,15] although the configuration is not in general used to test fracture properties.

3.2 *Bending tests*

From the CC perspective, bending tests differ significantly from tensile tests because a part of the specimen is under tension while the other one is in compression; thus, the stress condition cannot be fulfilled throughout the specimen. Failure occurs in two stages: crack initiation followed by crack growth, leading or not to the complete failure.
In the following, mm-scale (resp. µm-scale) means that units for the dimensions of the specimens (as shown in Figure 3) are mm (resp. µm). These two scales are the most relevant to ceramic testing. However, side studies to the cm- or nm-scale will also be made as well as to intermediate scales.

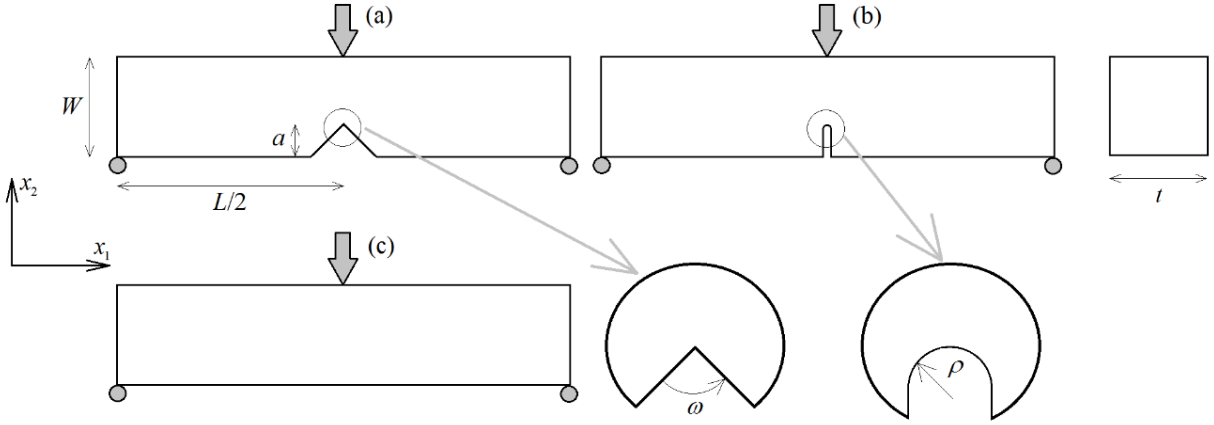

Figure 3. 3-point bending tests. (a) V-notched specimen, (b) U-notched specimen, (c) plain specimen: L = 8, W = 2, t = 2, a = 0.4. Units are not specified, they vary depending on the selected scale.

The analysis is performed in 2D plane strain elasticity. Using the above material data (Section 3.1), FE computations can be carried out once and for all whatever the scale, being aware that units for lengths vary. The only change to bring during the post-processing analysis is to modify the value of G_c (e.g. 0.023 MPa mm = 23 MPa µm) which reduces significantly the numerical effort.
Computations are conducted either with a prescribed vertical displacement $U_d = -1$ to simulate displacement-controlled (DC) loading mode or with a prescribed vertical force $F = -1$ for force-controlled (FC) loading mode (in both cases without prescribing the units). Thus, the stress field is unchanged whatever the units but the stress gradient through the specimen increases drastically descending the scales.

In addition, we introduce a physically significant parameter σ_f, baptized equivalent flexural strength, that allows comparisons between the various cases, it is the tensile stress that would prevail in the middle of the bottom face of the plain specimen (Figure 3c) undergoing the same bending load.

3.3 *Bending of a V-notched specimen*

Figure 4 compare the GSIF k at failure computed by the FFE approach (FC loading mode) to its critical value k_c deriving of the asymptotic procedure (Table 1) for sharp V-notched

specimens under 3-point bending. Not surprisingly, the two curves $\omega = 0$ deg. and $\omega = 30$ deg. merge because the singularity exponents are very close to each other (Table 1).

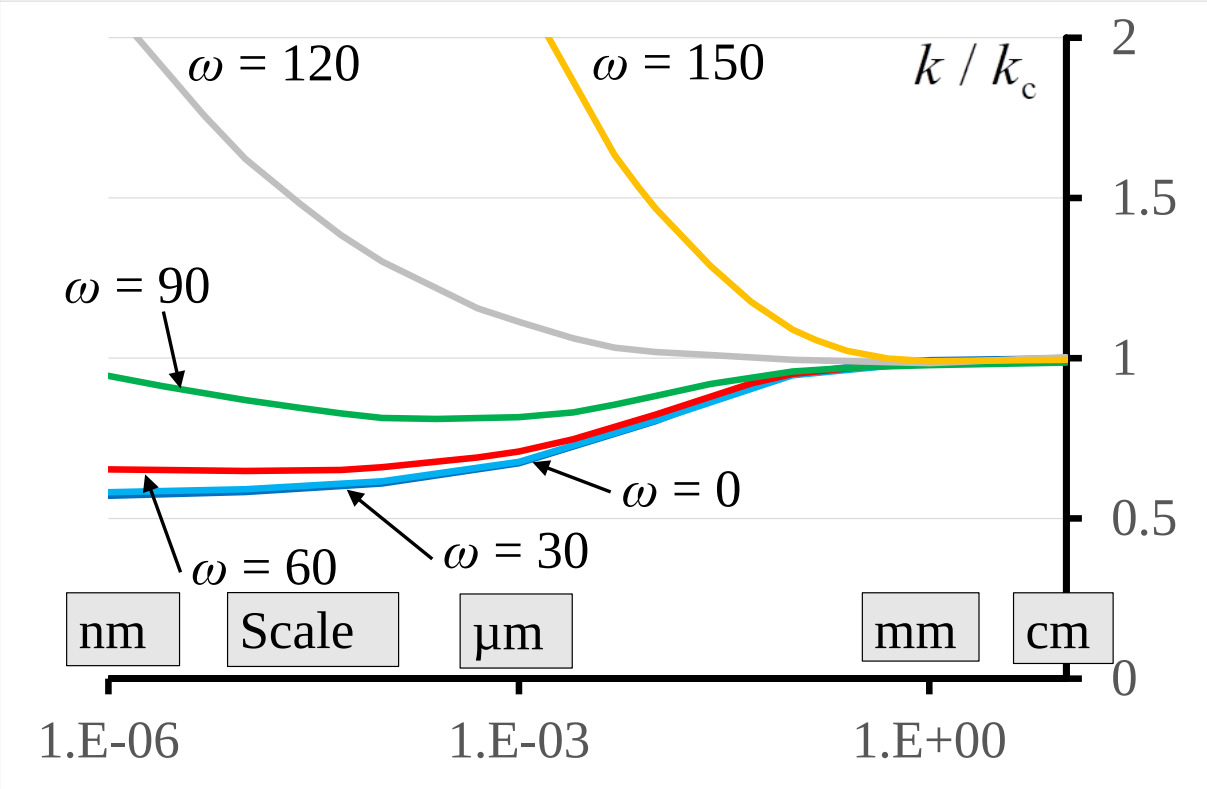

Figure 4. The ratio k / k_c between the GSIF at failure computed by FE (FC loading) and its asymptotic value for various opening angles.

Clearly, the asymptotic approach works well for any opening angle ω at the cm- and mm-scale. This is because the crack increment length at initiation δl remains smaller than 1 % of the ligament width $W - a$ and thus satisfies the smallness condition which validates the asymptotic expansions (Figure 5). Obviously, k deviates more and more significantly from k_c for scales below the mm-scale because the ratio of the initiation length δl to the ligament width no longer meets the condition of smallness. Indeed, the FFE approach considers the whole elastic solution, thus, higher terms in William's expansion (11), ignored in the asymptotic approach which retain only the leading term, become predominant as δl becomes bigger.

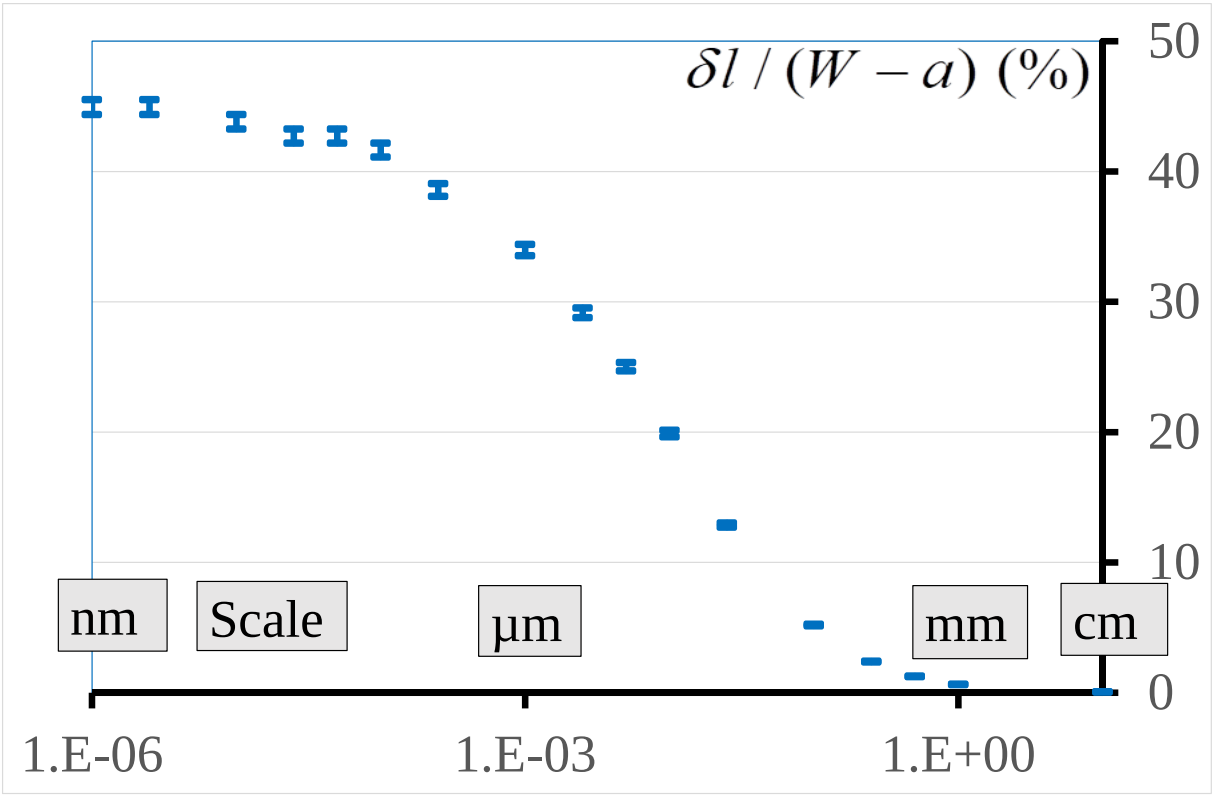

Figure 5. The ratio $\delta l / (W - a)$ at various scales for $\omega = 90$ deg. (FC loading). The error bars correspond to the mesh size.

This is obviously also true for a crack, as a consequence, using formulas derived from Griffith's criterion to determine the material toughness at the µm-scale risks to be unreliable. The same above trends exist but are less exacerbated in case of DC loading mode.

Table 2 summarizes the results obtained with a sharp V-notched specimen under FC loading mode. As already observed in Figure 4, the two cases $\omega = 0$ deg. and $\omega = 30$ deg. merge. Obviously, smaller the scale and smaller the influence of the geometry (this is more and more true when descending to the nm-scale although not shown here).

Table 2. The equivalent flexural stress σ_f at failure for the V-notch specimen under FC loading mode for different opening angles.

Scale (mm)	10	1	0.1	0.01	0.001
σ_f (MPa) $\omega = 0$ deg.	26.6	83.5	252.3	675.5	1786.7
σ_f (MPa) $\omega = 30$ deg.	26.6	83.7	252.3	675.5	1786.7
σ_f (MPa) $\omega = 60$ deg.	28.1	85.3	253.4	675.5	1786.7
σ_f (MPa) $\omega = 90$ deg.	32.7	92.4	258.2	677.7	1786.7
σ_f (MPa) $\omega = 120$ deg.	46.8	111.3	272.4	675.5	1786.7
σ_f (MPa) $\omega = 150$ deg.	82.6	145.6	283.3	675.5	1765.0

3.4 Bending of an unnotched specimen

It is in this configuration that the effects of the stress gradient are most noticeable (Figure 6) as can be observed in Table 3 with the dramatic increase of $\sigma = \sigma_{eq} > \sigma_c$ when moving from the cm-scale to the µm-scale.

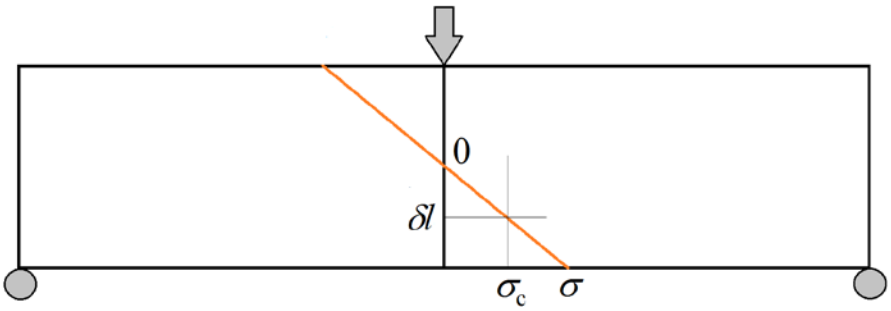

Figure 6. Schematic view of the stress gradient effects in a bending test. The red solid line is the tensile component of the stress tensor along the middle axis. It is positive on the bottom face and negative above.

Similar conclusions to the preliminary remark (Section 3.1) can be drawn. It is difficult to interpret these values as representative of a material bending strength. One can note that even at the cm-and µm-scale, σ differs from the tensile strength σ_c as was already highlighted in [30]. This was also observed in [31], although the study was conducted at the macroscopic scale, the thickness of a specimen in bending was varied and the effects of the stress gradient were evidenced.

Table 3. The tensile stress $\sigma = \sigma_{eq}$ that prevails at failure of the plain specimen in the middle of the bottom face.

Scale (mm)	10	1	0.1	0.01	0.001
σ (MPa) FC	401.4	414.0	518.6	980.5	2375.1
σ (MPa) DC	401.5	413.9	522.9	1122.7	3909.9

Without any statistical consideration on the presence and size of defects [32], we can observe in Table 3 an apparent strengthening of the material due to its smallness. Moreover FC and DC loading modes differ more and more significantly descending the scales.

3.5 *Bending of a U-notched specimen*

We will now focus on U-notched specimens (Figure 3b) which is the geometrical configuration closest to the fracture test conditions on ceramic specimens at both mm and µm scales.

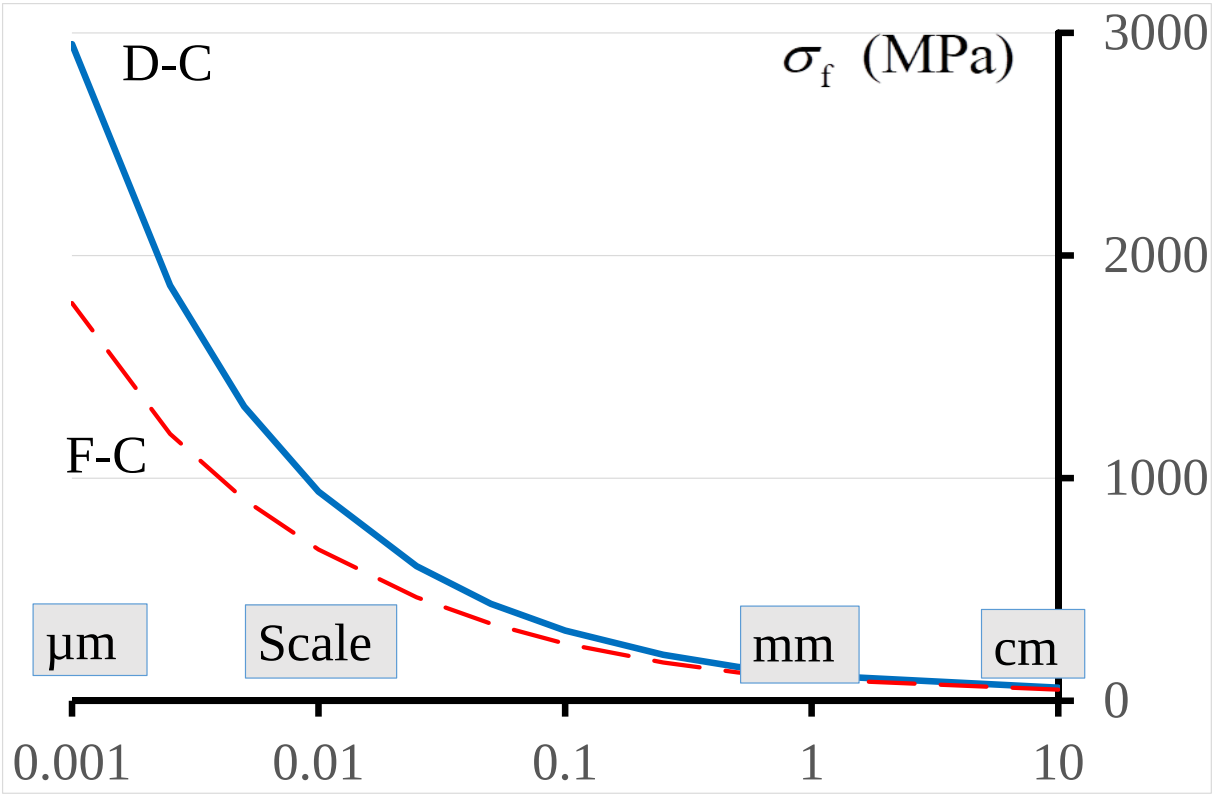

Figure 7. The stress σ_f at failure for the U-notch specimen with $\rho = 0.02$ at different scales.

Figure 7 shows the equivalent flexural stress σ_f at failure for U-notched specimens with $\rho =$ 0.02 (i.e. 0.02 mm at the mm-scale and 0.02 µm at the µm-scale). Results do not depend on how the load is applied at the cm- and mm-scale but the gap widens at smaller scales as already observed in Table 3. This result that could surprise can be explained by two different failure mechanisms. In the DC case, the IERR curve grows slowly and even pass through a maximum before decreasing. Then, there is initiation followed by a possible crack arrest at a shorter and shorter distance descending the scales because there is less and less energy to be released (see Figure 1b). While under FC loading mode, the IERR curve grows rapidly without further decay. There is initiation followed by unstable crack growth until complete failure (see Figure 1a). However, this is strongly related to the value of σ_c. If σ_c is higher, the red curve moves to the left in Figures 1a and 1b, then the situation becomes more classical with an increasing energy curve and a decreasing stress curve and the gap between the approaches tends to vanish. Let us add that this difference between DC and FC loading modes is not reserved to microscopic scales, the same phenomenon can be observed at macroscopic scale if σ_c is small and consequently the initiation length is large.

Table 4 summarizes the results for two different notch blunting ($\rho = 0.25 \times a = 0.1$ and $\rho = 0.05 \times a = 0.02$). Obviously, the influence of the blunting is more prominent at the larger scales. At the µm-scale the results almost merge with those of the V-notches (see Table 3).

Table 4. The equivalent flexural stress σ_f (MPa) at failure for the U-notch specimen under FC loading mode with $\rho = 0.1$ and $\rho = 0.02$ (units depend on the scale).

Scale (mm)	10	1	0.1	0.01	0.001
σ_f (MPa) $\rho = 0.1$	88.6	122.0	268.0	675.5	1765.0
σ_f (MPa) $\rho = 0.02$	49.9	97.0	257.1	679.8	1786.7

One conclusion to be drawn from these results is that at the µm-scale the exact shape of the notch plays a minor role. Only its depth a or more precisely the width of the remaining ligament $W - a$ is decisive. This conclusion is reinforced by a computation on a plain specimen whose width is $W - a$ instead of W, under FC loading mode it gives $\sigma_f = 1660.4$ MPa not far from the above values (Table 4). We draw attention to the fact that this value is not the one that prevails on the outer face of this thin plain specimen (usually denoted σ) but the one that would prevail on the thick plain specimen under the same load. This remarkable feature is also visible in Figures 8 and 9 below.
Such a property was already observed in [33] where it is noted that below a length scale the material (nacre) becomes insensitive to pre-existing flaws. It is concluded that Griffith criterion becomes inoperative and failure is governed by the theoretical strength. However, we disagree with this conclusion, the energy is still governing fracture and it is the small available amount that forces to increase the load.

3.6 *Influence of the fracture energy*

We will mainly focus now on the U-notched specimens with $\rho = 0.02$ and the plain specimens because the next sections will be dedicated to comparisons with experiments found in the literature which refer to this type of samples.

Figure 8 compares the equivalent flexural stress σ_f function of the fracture energy at the mm-scale and the µm-scale. As already noticed, the influence of the fracture energy is more pronounced at the µm-scale. However, at the mm-scale, the fracture energy still has some influence on the U-notched specimens while it is weaker for the plain specimens.

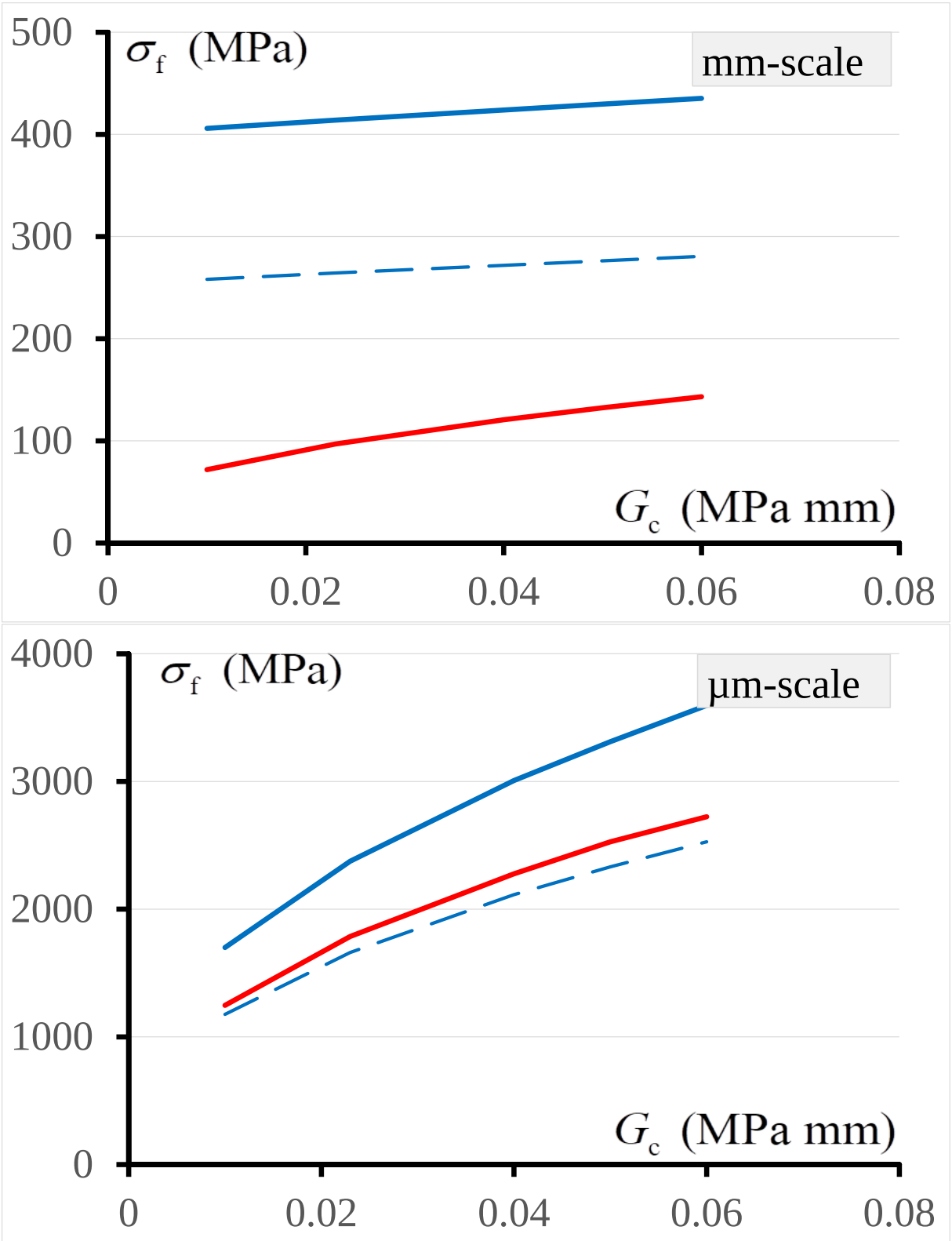

Figure 8. The stress σ_f function of the fracture energy G_c at the mm-scale and the µm-scale for the U-notched specimen with $\rho = 0.02$ (red solid line), for the plain specimen with height $W = 2$ (blue solid line) and for the plain specimen with height $W - a = 1.6$ (blue dashed line). Computations are carried out under FC loading.

3.7 *Measuring the toughness from the bending test*

With the data used above (Section 3.1), it comes $K_{Ic} = 3.03$ MPa m$^{1/2}$. Usually, the notch is considered, whatever its acuity, as a crack and the toughness is derived from the load at failure F_c using the following analytical formulas [34]

$$K_{Ic} = \bar{\sigma}\sqrt{\pi a}\, f(a/W) \text{ with } \bar{\sigma} = \frac{6F_c L}{4W^2} \text{ and}$$
$$f(a/W) = \frac{1}{\sqrt{\pi}} \frac{1.99 - a/W(1-a/W)(2.15 - 3.93a/W + 2.7(a/W)^2)}{(1+2a/W)(1-a/W)^{3/2}} \quad (18)$$

Table 5 shows the toughness K_{Ic} (MPa m$^{1/2}$) calculated using (18) and the load at failure predicted by the CC for various specimens under FC loading mode. Obviously, at the macro-scale (i.e. cm-scale and mm-scale), Tada's formula and CC predictions of failure lead to an error not exceeding 2% for sharp notches with $\omega \leq 30$ deg. The result is getting worse for larger opening angles and even becomes completely wrong for a strongly blunted U-notch with $\rho =$ 0.02 at the cm-scale (i.e. $\rho = 0.02$ cm).

Table 5. The toughness K_{Ic} (MPa m$^{1/2}$) using (18) and the load at failure predicted by the CC for various V-notched and U-notched specimens under FC loading mode, compared to the actual value (right column).

Specimen→ Scale (mm)↓	$\omega = 0$ deg.	$\omega = 30$ deg.	$\omega = 60$ deg.	$\omega = 90$ deg.	$\rho = 0.02$	Actual value
10	3.08	3.08	3.26	3.79	5.78	3.03
1	3.06	3.07	3.13	3.39	3.55	3.03
0.1	2.92	2.92	2.94	2.99	2.98	3.03
0.01	2.48	2.48	2.48	2.48	2.49	3.03
0.001	2.07	2.07	2.07	2.07	2.07	3.03

At the macro-scale the calculation tends to overestimate the actual value. This trend is reversed at smaller scales, the actual value is now underestimated by 32% at the µm-scale. Moreover, as already mentioned, the exact shape of the notch no longer plays any role. This conclusion is consistent with that of subsection 3.3.

3.8 *Influence of the tensile strength*

Figure 9 shows the equivalent flexural strength stress σ_f function of the tensile strength σ_c at the mm-scale and the µm-scale. The tensile strength has a big influence on the plain specimens at the mm-scale, σ_f scales approximately linearly with σ_c. This is no longer true at the µm-scale even if the influence of σ_c remains significant, the energy condition takes precedence.

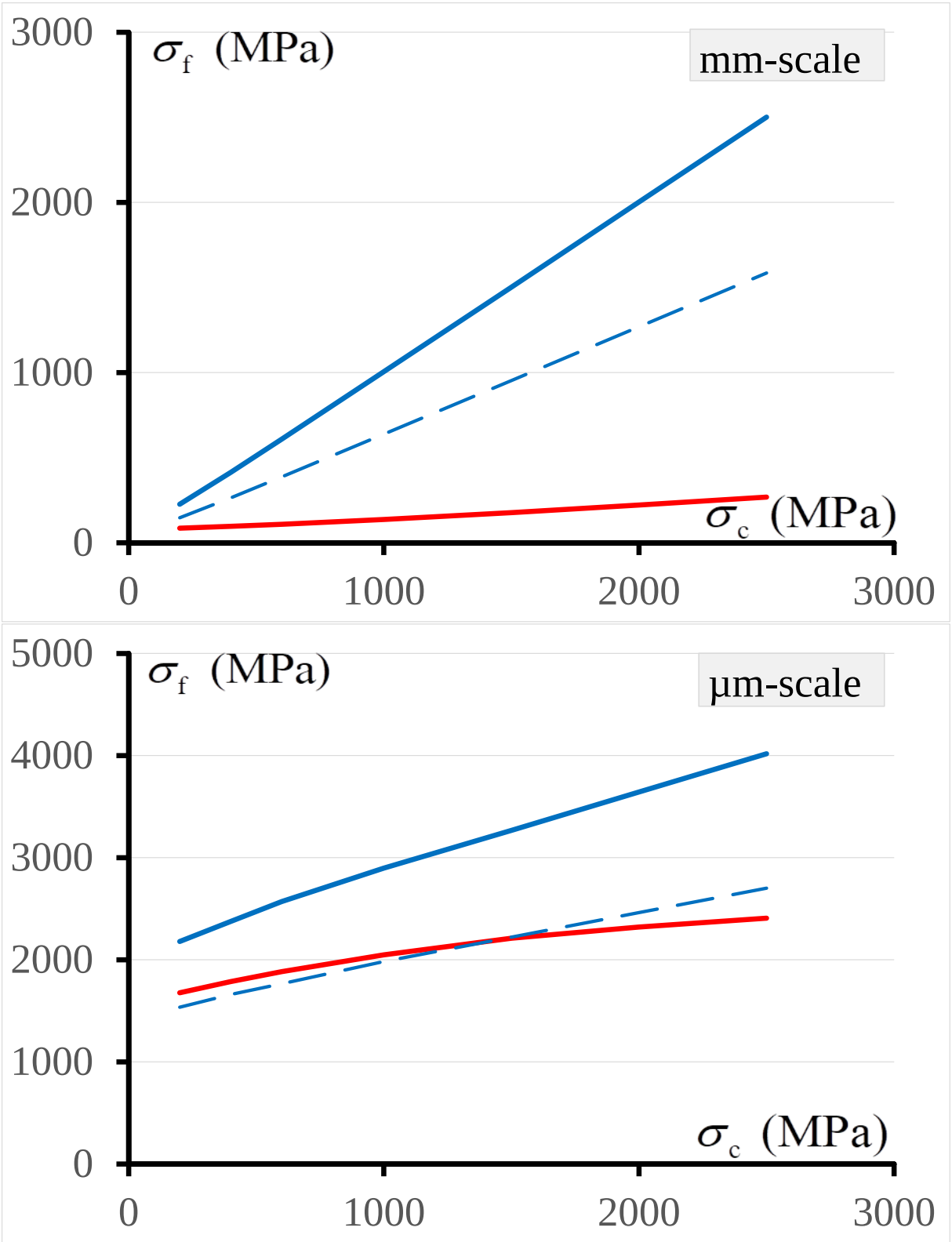

Figure 9. The stress σ_f function of the tensile strength σ_c at the mm-scale and the µm-scale for the U-notched specimen with $\rho = 0.02$ (red solid line), for the plain specimen with width $W = 2$ (blue solid line) and for the plain specimen with width $W - a = 1.6$ (blue dashed line). Computations are carried out under FC loading mode.

4. Comparison with micro-scale experiments

4.1 *Comparison with Henry's experiments on zirconia*

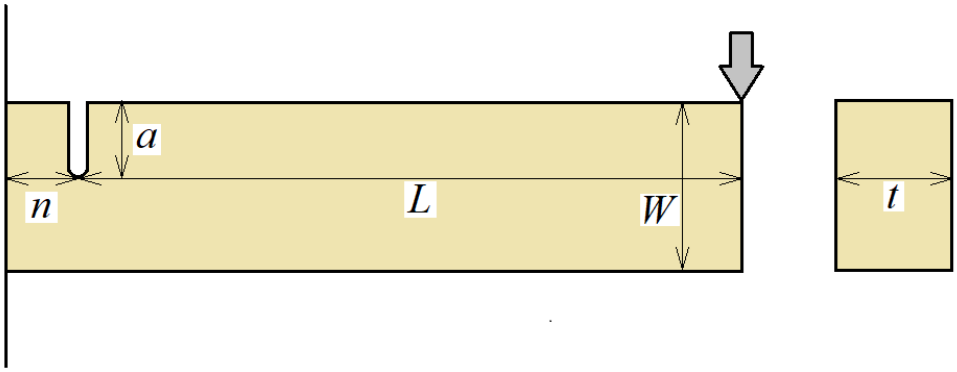

Figure 10. The U-notched micro-cantilever beam.

Using a micro-indenter, Henry et al. [35] carried out bending tests on notched micro-cantilever beams (Figure 10) made of a ceramic material 8Y-FSZ cubic zirconia (E = 216 GPa, ν = 0.22). Beams were milled with a FIB and remained clamped to a part of bulk material. On micrographs, the specimen appears smooth and free of surface defects.
After having noted the very small difference between the case of a beam clamped at its end and a more complete simulation including a part of the bulk material, the first case was retained in the computations for simplicity.
The geometry of the beam cross section is pentagonal since it can be more easily milled, such geometry cannot be reproduced in a 2D model. However, according to [36] results are very similar to the ones obtained by a rectangular cross section. Thus, the height of the specimen W in the simulation is set as the height of the rectangular part plus one half of the height of the triangular part of each micro-beam. The U-notch radius is 0.01 µm. Dimensions related to the 14 specimens are given in Table 6. It can be noted that the difficulty of milling the specimens leads to a certain dispersion of the geometry.

Table 6. Geometrical parameters of the 14 different specimens tested in [35]. All the parameters are in µm. Tests are carried out under FC loading mode except those with a * done under DC loading mode.

Index	L	W	t	n	a	Index	L	W	t	n	a
1	9.20	4.34	5.98	0.920	1.32	8	8.76	4.30	4.99	0.876	0.50
2	9.97	4.04	4.99	0.997	0.64	9	8.13	4.57	5.34	0.813	0.42
3	9.74	5.01	6.27	0.974	0.70	10	7.19	4.12	3.45	0.719	0.84
4	9.10	4.66	6.21	0.910	0.61	11	7.33	4.60	4.18	0.733	0.56
5	8.03	4.20	4.57	0.803	0.56	12	9.40	4.13	4.56	0.940	0.70
6*	8.76	4.26	4.42	0.876	0.91	13	7.08	4.35	5.25	0.708	0.83
7*	12.11	3.32	4.40	1.211	0.64	14*	9.96	3.50	3.94	0.996	0.63

A global least square method allows computing the best fit pair $(\tilde{\sigma}_c, \tilde{G}_c)$

$$\tilde{\sigma}_{ic}, \tilde{G}_{ic} = \text{argmin} \sum_{i=1}^{14} \left(F_i^{\text{sim}}(\sigma_c, G_c) - F_i^{\text{exp}} \right)^2 \tag{19}$$

where $F_i^{\text{sim}}(\sigma_c, G_c)$ is the applied load at which the CC is fulfilled according to the simulations and F_i^{exp} is the measured fracture load, for the i-th specimen. The range for G_c is 2 to 20 J m^{-2} (step 0.5) and for σ_c 0.4 to 8 GPa (step 0.2). It gives $\tilde{G}_c = 10.5$ J m^{-2} and $\tilde{\sigma}_c = 5600$ MPa under DC loading mode and $\tilde{G}_c = 9.5$ J m^{-2} and $\tilde{\sigma}_c = 7400$ MPa under FC loading mode. Obviously, there is an important difference in the evaluation of σ_c and the search for an optimal pair $(\tilde{\sigma}_{ic}, \tilde{G}_{ic})$ case by case can be carried out allowing a better perception of the scattering

$$\tilde{\sigma}_{ic}, \tilde{G}_{ic} = \text{ argmin } \left(F_i^{\text{sim}}(\sigma_c, G_c) - F_i^{\text{exp}} \right)^2 \text{ for } i = 1,14 \tag{20}$$

Results are given in Table 7 under FC loading mode, except specimens 6, 7 and 14 (marked with a *) under DC loading mode like in experiments. Clearly, there is a wider scattering in the determination of the tensile strength than in that of the fracture energy, leading to the average values $\overline{G}_c = 10.3$ J m^{-2} and $\overline{\sigma}_c = 4000$ MPa, excluding or not specimens 4 and 8 which does not make a big difference. In this regard, a comparison between Henry et al. estimates [35] of the material toughness K_{Ic} and the present analysis shows that, precisely as in our identification of G_c, the minimum is found for sample 4 and the maximum for sample 8 (Figure 11). Thus, these extreme values seems not to be an inconsistency of the CC.

Table 7. Estimation of the fracture energy $\tilde{G}_{ic}$ and tensile strength $\tilde{\sigma}_{ic}$ for each specimen. Specimens 4 and 8 seems to be a bit out of the general trend.

Index	$\tilde{G}_{ic}$ (J m^{-2})	$\tilde{\sigma}_{ic}$ (GPa)	Index	$\tilde{G}_{ic}$ (J m^{-2})	$\tilde{\sigma}_{ic}$ (GPa)
1	8.5	5.0	8	18.5	1.6
2	11.0	3.8	9	13.5	4.4
3	11.5	4.6	10	7.0	5.4
4	4.0	7.8	11	9.0	1.0
5	12.0	4.0	12	10.5	1.6
6*	10.0	3.0	13	8.5	1.6
7*	12.5	7.4	14*	7.5	4.4

Note that the minimization of the relative error

$$\tilde{\sigma}_c, \tilde{G}_c = \text{ argmin } \sum_{i=1}^{14} \left(\frac{F_i^{\text{sim}}(\sigma_c, G_c) - F_i^{\text{exp}}}{F_i^{\text{exp}}} \right)^2 \tag{21}$$

gives a close result to (19) in terms of fracture energy: $\tilde{G}_c = 9$ J m^{-2}, but a significant difference in term of tensile strength: $\tilde{\sigma}_c = 7000$ MPa, emphasizing the difficulty to determine the tensile strength with this kind of experiment. Of course, in the local process (20), absolute and relative errors make no difference.

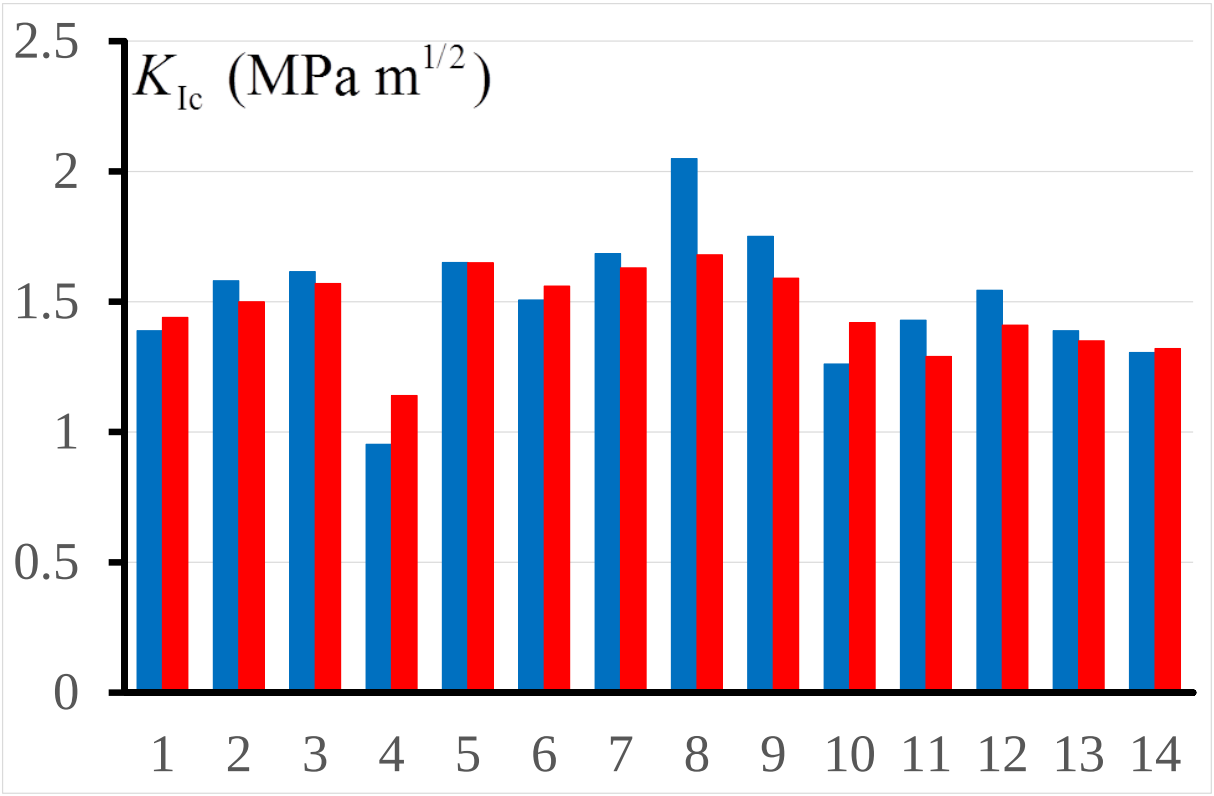

Figure 11. Comparison on the identification of the material toughness K_{Ic} between the present analysis (blue) and Henry et al. [35] estimates (red) for the 14 specimens.

To conclude, there is a good agreement with the global minimization on the fracture energy but a poor one on the tensile strength. This can be explained, as already mentioned, by a low sensitivity of the CC to σ_c at the micro-scale. This is visible in Figure 12 (specimen 1 under FC loading mode) where the different fracture energies result in curves that are quite distinct from each other (left), while different tensile strengths give curves that have a clear tendency to overlap. This trend is even more pronounced in the case of DC loading mode.
On the contrary, a fracture energy around 10 J m^{-2} seems to be confirmed by the different approaches.

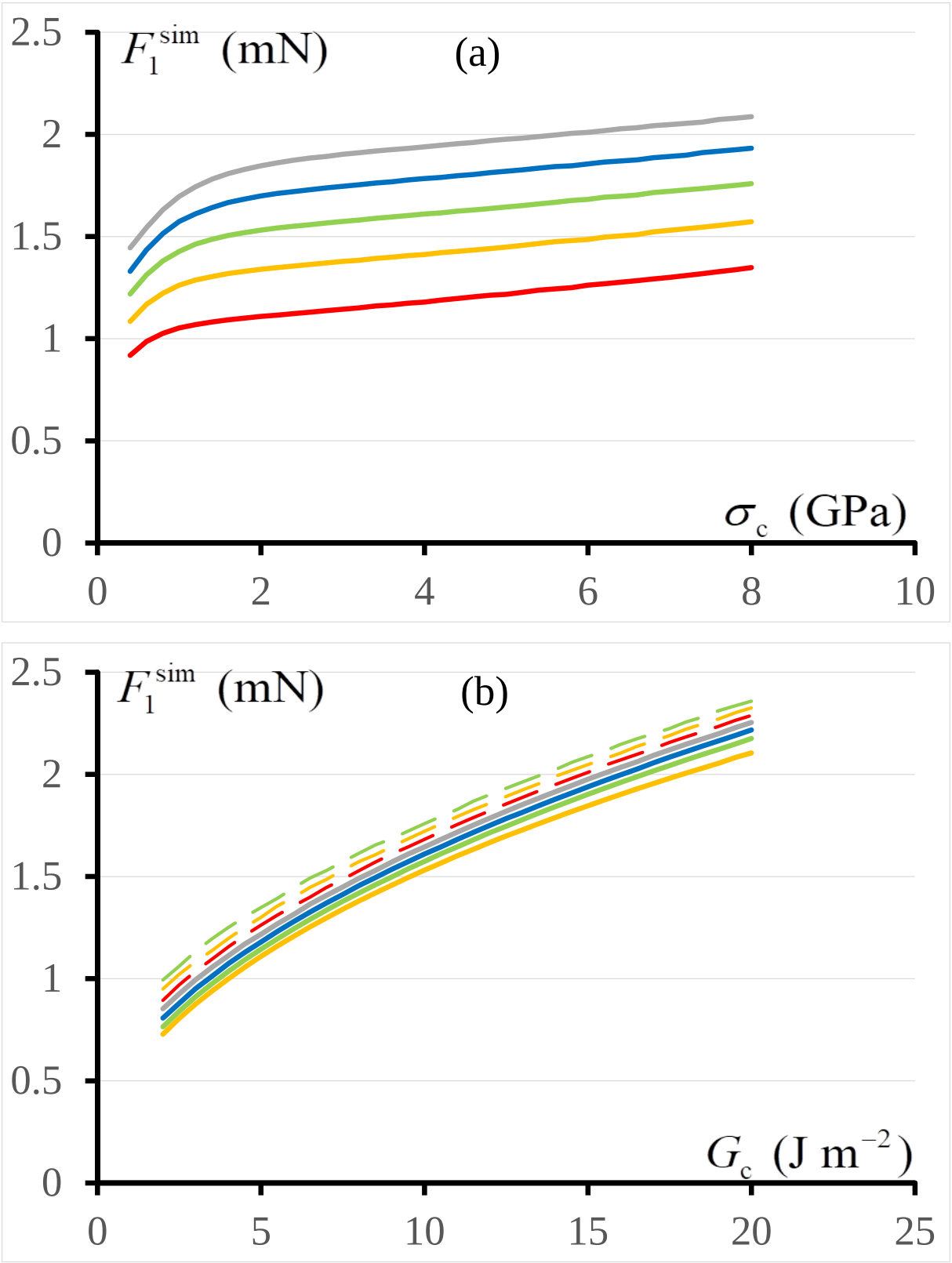

Figure 12. The critical applied force at failure on specimen 1 under FC loading mode using the CC, (a): function of the tensile strength for various values of the fracture energy from 2 to 15 J m^{-2} step 2.5 (bottom to top); (b): function of the fracture energy for various tensile strength from 1 to 8 GPa step 1 (bottom to top).

4.2 *Comparison with Pejchal's experiments on alumina*

Pejchal et al. [37] carried out bending experiments on a C-shaped specimen extracted from a single grain of alumina ($E = 400$ GPa, $\nu = 0.25$, $K_{Ic} = 3$ MPa m$^{1/2}$ ($G_c = 0.021$ MPa mm)). The specimen is fixed to a polymer support ($E = 1$ GPa, $\nu = 0.25$), as illustrated in Figure 13. Since the polymer Young's modulus is far smaller than that of the alumina specimen, the size of the polymer support is adjusted to have the same stiffness in the current simulations (based on a linear elastic model) and the experiments (see Figure 14).

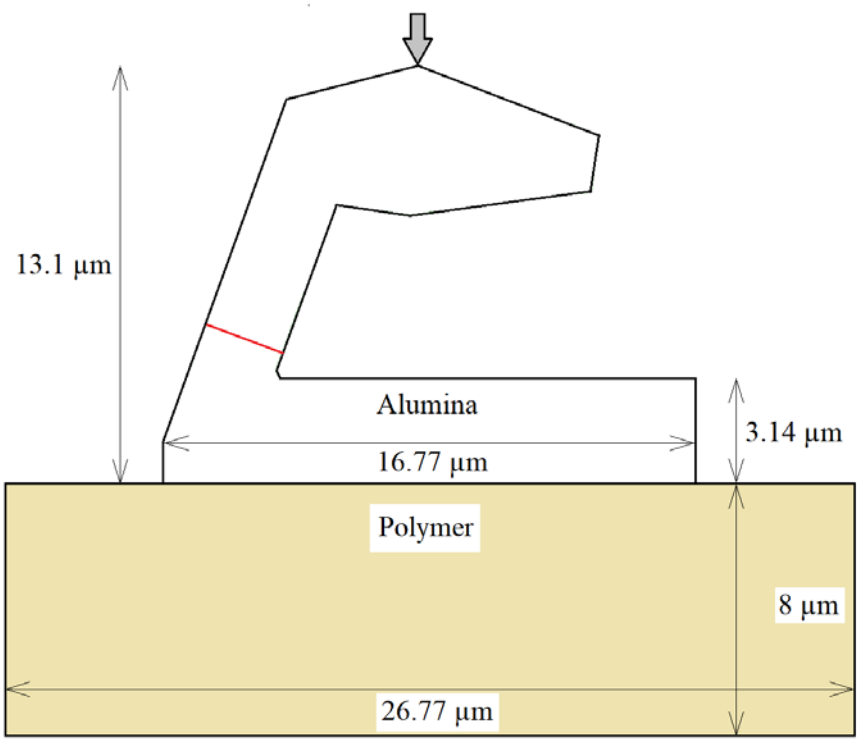

Figure 13. C-shaped specimen in bending, in red the presupposed crack path. Some dimensions are given as an indication. Please refer to [37] for the detailed geometry. The specimen thickness is assumed to be 5 µm.

The authors report a horizontal as well as a vertical component of the applied force, so a vertical displacement is imposed to the top point of the sample while inhibiting the horizontal displacement. This leads to a ratio between the horizontal and vertical components of the applied force of 0.17 while the authors measured approximately 0.1 (it is not excluded that a small slip occurs under the indenter). The presupposed crack path is orthogonal to the surface of the left face of the beam and located at the point of maximum tension.

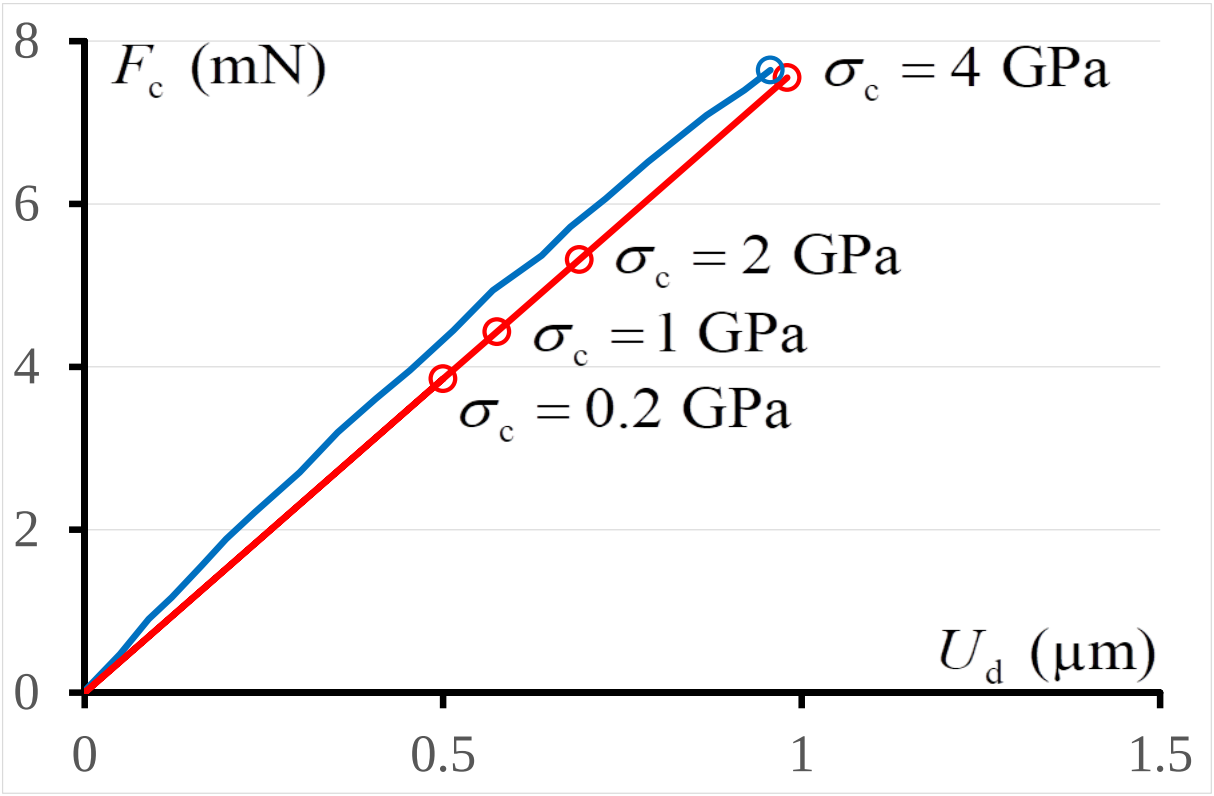

Figure 14. The applied force at failure function of the prescribed displacement. The blue solid line is the loading curve, the red solid one is the simulated one. The blue circle corresponds to the specimen failure in the experiments. The red circles are the failure loads predicted by the CC for various tensile strength values σ_c.

Figure 14 shows the predicted failure loads using the CC for different values of the tensile strength σ_c compared to the experimental loading curve. A satisfying matching is obtained for $\sigma_c = 4$ GPa. However, it can be observed that the load at failure is only twice (4 to 8 mN) while the tensile strength is multiplied by 20 (0.2 to 4 GPa), reflecting a low dependence of the result on the tensile strength (remember that it scales more or less linearly at the macro-scale for an unnotched specimen (Figure 6)).

In Table 7, the tensile stress σ prevailing at the breaking point at specimen failure can be compared to the tensile strength σ_c. For a small σ_c, σ is far above, it is a new proof of the influence of the stress gradient since the crack initiation length is large compared to the beam thickness (column 3). As σ_c increases, the gap decreases together with the initiation length and the Irwin length l_{Irwin}. The currently computed value of σ at failure underestimates the values reported in [37] which are baptized local strength and estimated around 10 GPa. They carried out non-linear elasticity computations based on large deformations while linear elasticity is presently used, but this does not seem sufficient to explain the difference since the loading curve only slightly deviates of the straight line.

Table 7. The tensile stress σ prevailing at the breaking point at specimen failure, function of the tensile strength σ_c. The crack length at initiation is in the third column together with the fraction of beam thickness and compared to the Irwin length (13).

σ_c (MPa)	σ (MPa)	δl (µm)	l_{Irwin} (µm)
200	2564.6	1.070 (42.9 %)	225
1000	2949.3	0.743 (29.8 %)	9
2000	3539.1	0.491 (19.7 %)	2.25
4000	5026.6	0.214 (8.6 %)	0.56

Figure 15 shows the pairs (G_c, σ_c) which provide the same critical displacement U_d than in experiments. Obviously, there is a wide range of values, both of σ_c and G_c. An experiment of a different type would be needed that could remove the uncertainty.

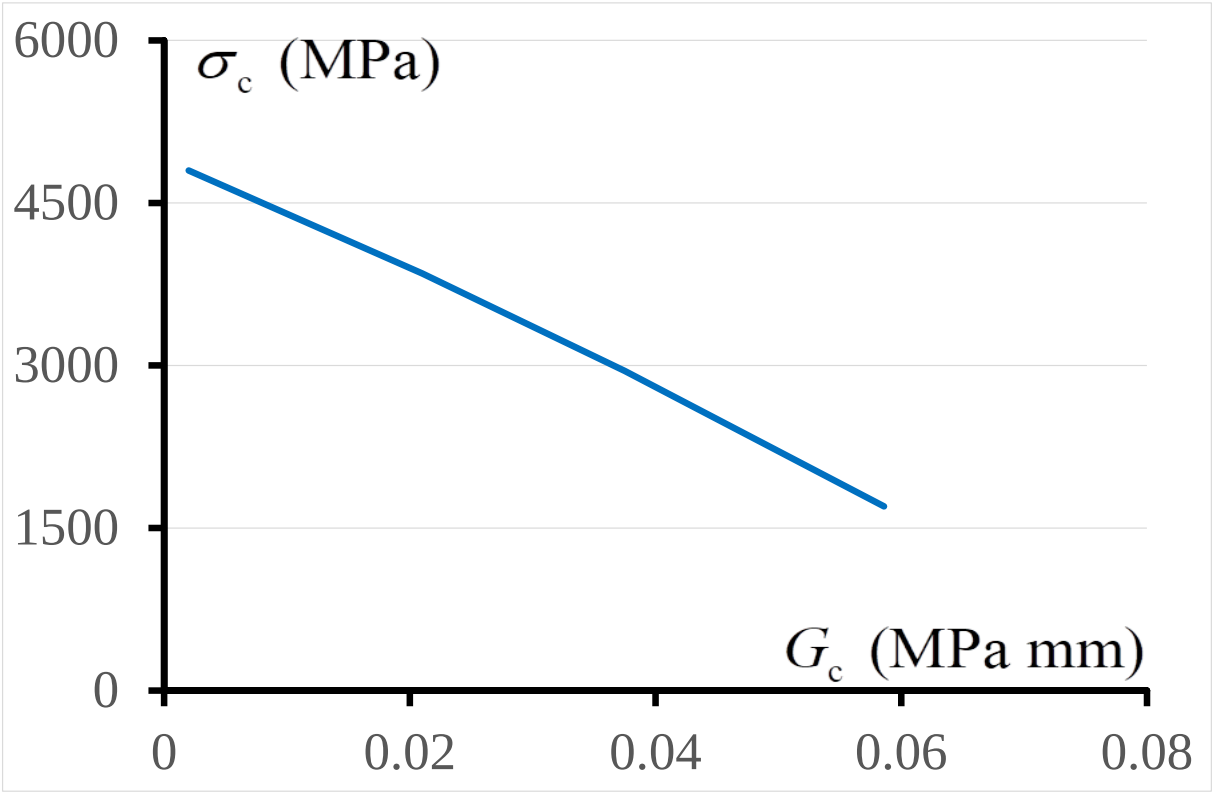

Figure 15. The pairs (G_c, σ_c) (fracture energy, tensile strength) leading to the same critical displacement U_d than in experiments.

4.3 *Comparison with Patil's simulations on aragonite*

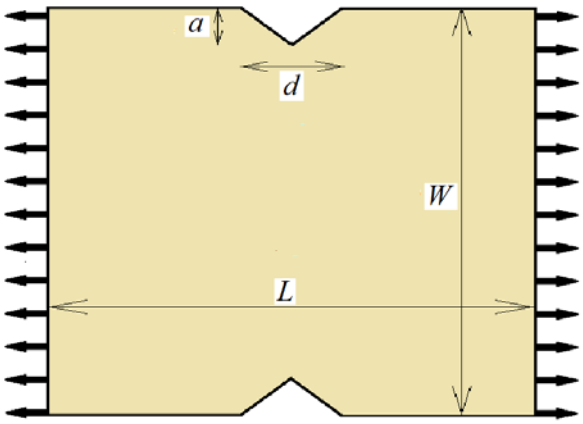

Figure 16. Double edge notched specimen of aragonite. L = 15.3 nm, W = 11.2 nm, d = 3.08 nm, a = 1.84 nm.

Even if they are invoked in [3], tests at the nano-scale are likely to be very difficult to perform. Patil et al. [38] propose only simulations of traction tests on nano-platelets of aragonite (Figure 16) using either molecular dynamics (MD) or phase field (PF) method. The reported material properties are $E = 126$ GPa, $\nu = 0.44$, $G_c = 2.091$ J m^{-2}.

The MD simulations tend to show that a crack initiates non-symmetrically at the tip of one of the notches and grows toward the other. It is this mechanism that is reproduced in the PF and CC simulations. In order to avoid non-linear elasticity and to carry out simplified linear elastic computations, the Young modulus have been readjusted to $E = 96$ GPa to have a similar global stiffness (see Figure 17).

Results shown in Figure 17 exhibit a satisfying agreement between MD, PF and CC simulations. For the CC, they are obtained after having adjusted $\sigma_c = 5$ GPa. The CC predictions under DC and FC loading modes differs because of different modes of failure. This is due to the special shape of the stress curve, decreasing then increasing because of the two symmetric notches, and to a slowly increasing energy curve in case of DC loading mode as shown in Figure 1c. The energy condition is fulfilled for a crack jump corresponding to the whole width of the ligament between the two notches and the stress condition is then $\sigma \geq \sigma_c$ through the whole ligament. There is only an initiation stage and the specimen is fully broken. While, in case of FC loading mode, the energy curve increases more rapidly and the situation is that of Figure 1a. There is a first stage of initiation where σ is not needed to be larger than σ_c through the whole ligament but only along the initiation length, followed by an unstable crack growth due to the FC loading mode.

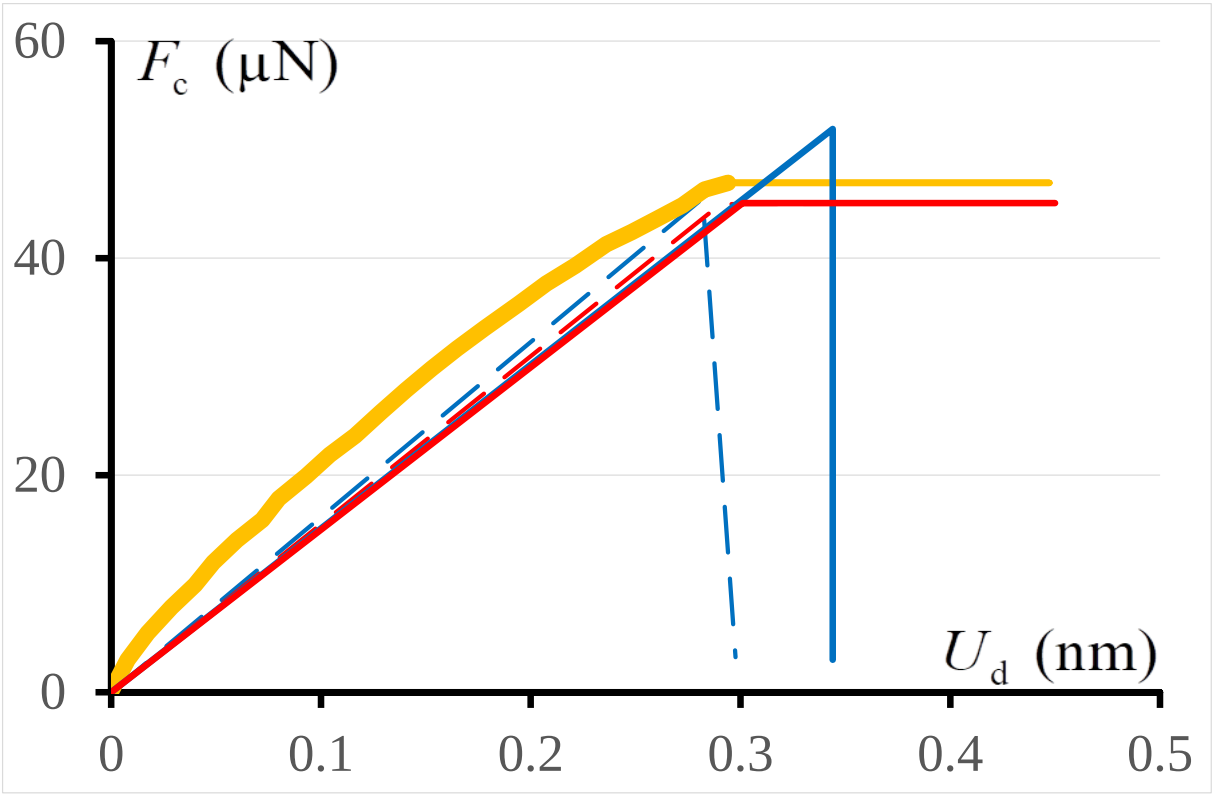

Figure 17. Simulation of failure of the nano-platelet of aragonite. MD: orange solid line, PF under DC loading: blue dashed line, PF under FC loading: red dashed line, CC under DC: blue solid line, CC under FC: red solid line. Results are obtained with $\sigma_c = 5$ GPa.

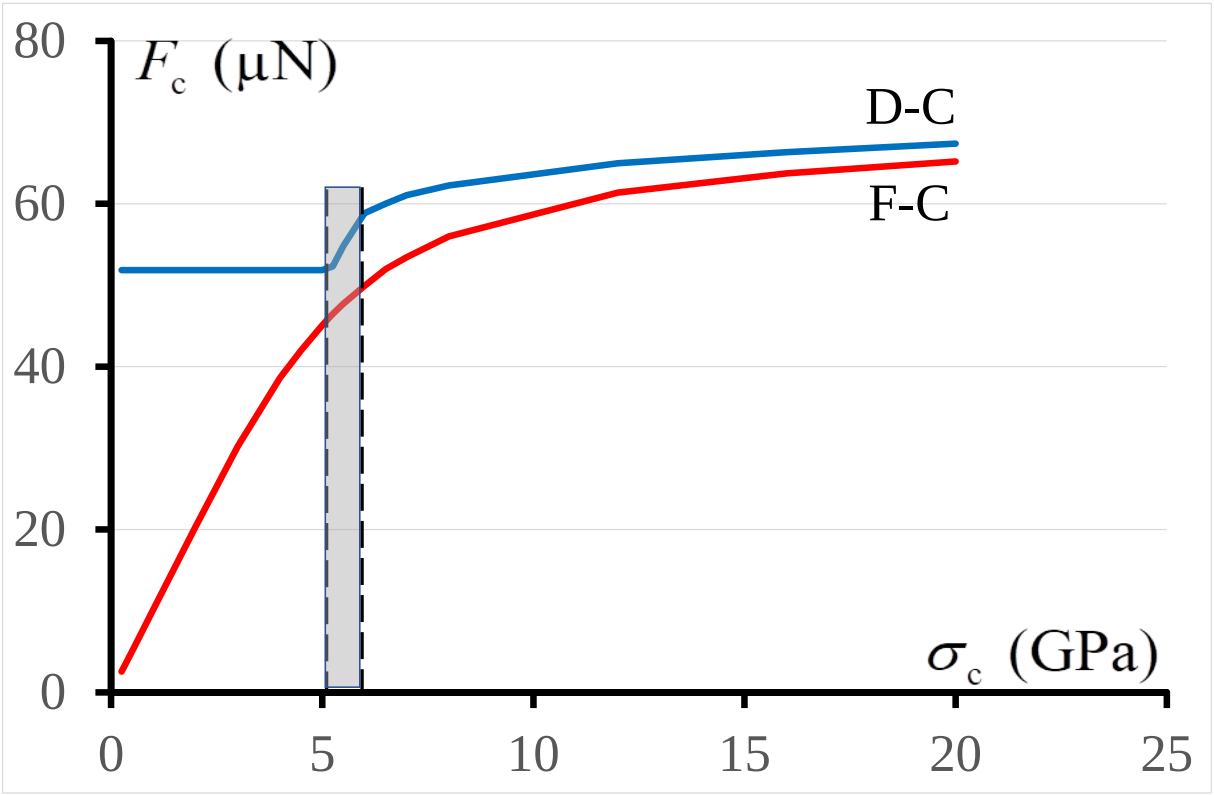

Figure 18. The predicted failure force, according to the CC, as a function of the tensile strength, under DC (blue solid line) and FC (red solid line) loading modes. At the left of the grey zone

failure under DC loading mode is entirely governed by the energy, inside the grey zone it is stress driven and on the right it is a mixed of the two conditions. Under FC loading mode the mixed conditions govern for the whole range of the parameter σ_c.

In Figure 18, it appears clearly that, according to the CC, in case of DC loading mode, the test is weakly sensitive to the tensile strength. It even becomes completely insensitive if $\sigma_c < 5$ GPa, while it remains sensitive under FC loading mode.
An interesting point to emphasize is that, under DC loading mode, the CC moves from a criterion entirely governed by the energy for $\sigma_c < 5$ GPa (Figure 1c), to a stress driven criterion for 5 GPa < $\sigma_c < 6$ GPa (Figure 19a) and to a classical mixed stress and energy condition for $\sigma_c > 6$ GPa (Figure 19b).
This test recalls the example of the bar in tension (Subsection 3.1) but with some differences due to the presence of the two notches. As a consequence, this test, especially under DC loading mode, seems again unsuitable for measuring any tensile strength.

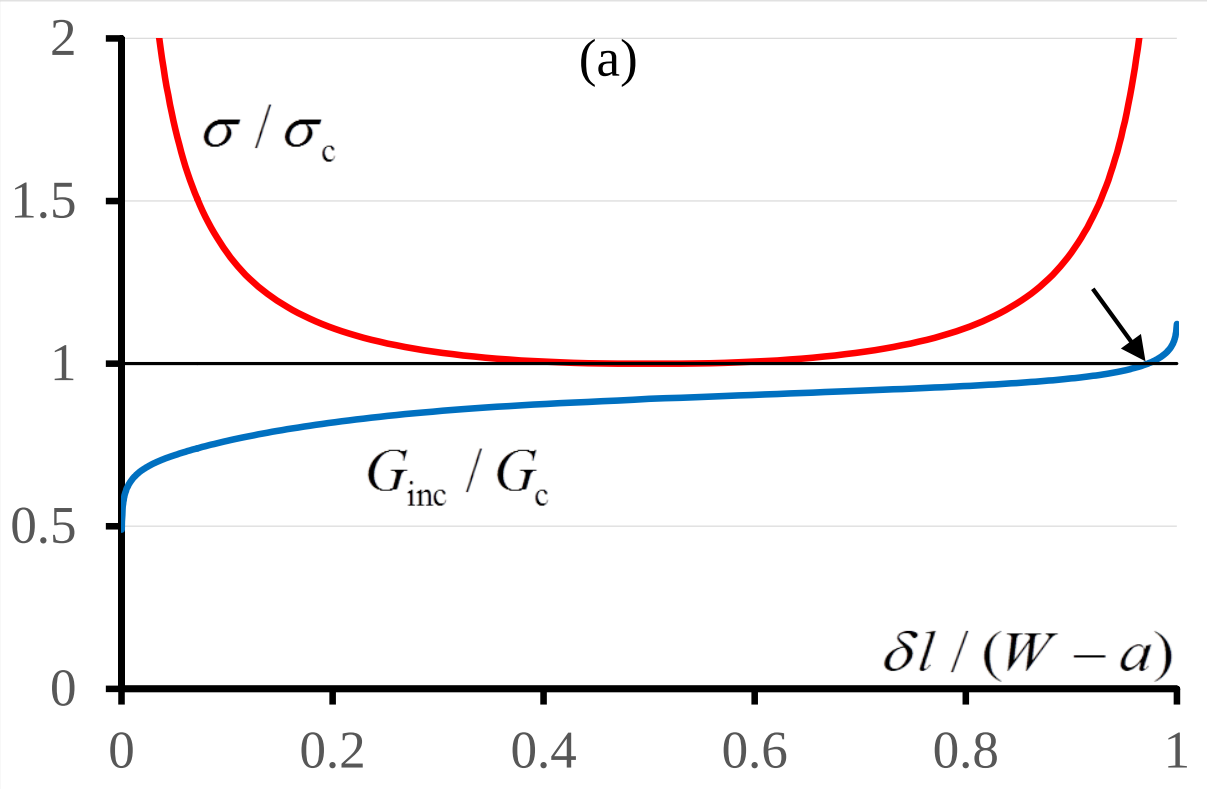

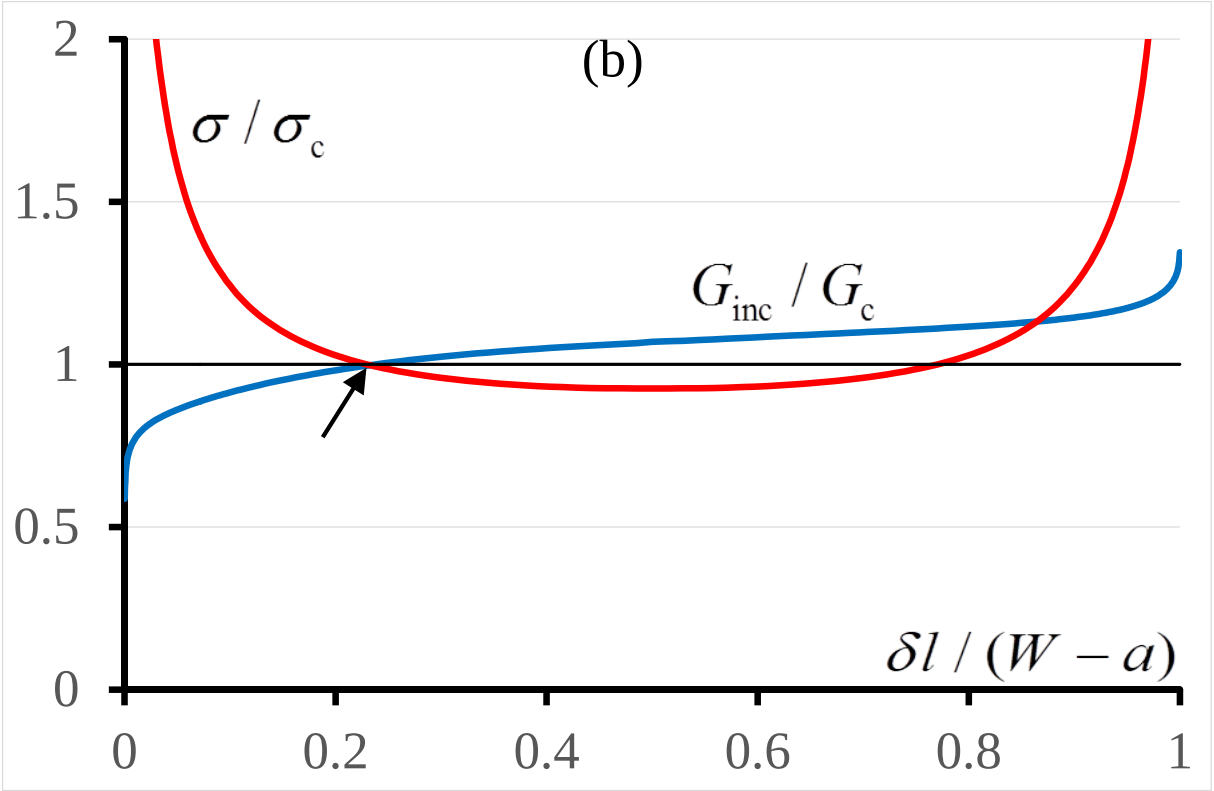

Figure 19. Two different applications of the CC under DC loading mode. (a) A stress driven criterion for σ_c = 5.5 GPa. (b) A mixed stress and energy condition for σ_c = 6.5 GPa. This is to be compared to Figure 1c obtained in the same conditions for σ_c = 5 GPa.

5. Conclusion

At the micro-scale, the CC must be used in its FFE form because the necessary condition of the asymptotic approach is no longer fulfilled. This prevents to use analytical formulas based on Williams's expansion.

The CC allows to show that the apparent strengthening observed in experiments conducted at the micro-scale is due to a lack of available energy as a consequence of the small size of the samples. In addition, in bending tests, the smaller the samples, the larger the stress gradient, leads to a similar apparent strengthening. It is often misinterpreted as an actual strengthening, although it has been shown in thin films, by varying the thickness of the film, that the tensile strength does not reach such high values [39,40].

Accordingly, tests are often weakly or even totally insensitive to the tensile strength whereas they are sensitive to the fracture energy. Moreover, the smaller the samples, the more insensitive they are to notches. It can be also noted that the effect of force and displacement controlled loading modes differs more and more descending the scales.

From the point of view of fracture mechanics, the concept of macro- and micro-scale could be refined based on the foundation of the CC: the discontinuous crack growth at onset over a finite length. At the macro-scale, this length is small compared to any dimension of the structure while at the micro-scale, it is of the same order of magnitude or even larger and can interact with the dimensions of the structure. This definition leads to a few mm and above for the macro-scale and a few µm and below for the micro-scale for alumina. But, according to the previous remark, the “microscopic” scale starts at a few cm and below for a rock like limestone (the Irwin length is around 30 cm) while the macroscopic scale is above 3 m.

Acknowledgements: The authors acknowledge the funding received from the European Union's Horizon 2020 research and innovation programme under the Marie Skłodowska-Curie grant agreement No 861061 – Project NEWFRAC.
The authors are also indebted to Roman Papsik, Josef Schlacher and Raul Bermejo for their knowledge of micro-scale experiments which they kindly shared.

References

[1] Gallo P., Sapora A. Brittle Failure of Nanoscale Notched Silicon Cantilevers: A Finite fracture Mechanics Approach. Appl. Sci. 2020; 10: 1640.
[2] Matoy K., Schönherr H., Detzel T., Schöberl T., Pippan R., Motz C., Dehm G. A comparative micro-cantilever study of the mechanical behavior of silicon based passivation films. Thin Solid Films 2009; 518: 247-256.
[3] Dehm G., Jaya B.N., Raghavan R., Kirchlechner C. Overview on micro- and nanomechanical testing: New insights in interface plasticity and fracture at small length scales. Acta Mater. 2018; 142: 248-282.
[4] Pardoen T., Colla M.S., Idrissi H., Amin-Ahmadi B., Wang B., Schryvers D., Bhaskar U.K., Raskin J.P. A versatile lab-on-chip test platform to characterize elementary deformation mechanisms and electromechanical couplings in nanoscopic objects. C.R. Phys. 2016; 17: 485-495.
[5] Henry, R., Zacharie-Aubrun, I., Blay, T., Chalal, S., Gatt, J. M., Langlois, C., & Meille, S. Fracture properties of an irradiated PWR UO2 fuel evaluated by micro-cantilever bending tests. J. Nuclear Materials 2020; 538: 152209.
[6] Doitrand A., Henry R., Zacharie-Aubrun I., Gatt J.M., Meille S. UO2 micron scale specimen fracture: Parameter identification and influence of porosities. Theor. Appl. Fract. Mech. 2020; 108: 102665.
[7] Doitrand A.,_Henry R., Saad H., Deville S., Meille S. Determination of interface fracture properties by micro- and macro-scale experiments in nacre-like alumina. J. Mech. Phys. Solids 2020; 145: 104143.
[8] Doitrand A., Henry R., Chevalier J., Meille S. Revisiting the strength of micron-scale ceramic platelets. J. Amer. Ceram. Soc. 2020; 103(12): 6991-7000.
[9] Binnig, G., Rohrer, H., Gerber, C., & Weibel, E. Surface studies by scanning tunneling microscopy. Phys. Rev. Letters 1982; 49(1): 57.
[10] Pethicai, J. B., Hutchings, R., & Oliver, W. C. Hardness measurement at penetration depths as small as 20 nm. Phil. Mag. A 1983; 48(4): 593-606.
[11] Di Maio, D., & Roberts, S. G. Measuring fracture toughness of coatings using focused-ion-beam-machined microbeams. J. Mat. Res. 2005; 20(2): 299-302.
[12] Norton A.D., Falco S., Young N., Severs J., Todd R.I. Microcantilever investigation of fracture toughness and subcriticalcrack growth on the scale of the microstructure in Al2O3. J. Eur. Ceram. Soc. 2015; 35: 4521-4533.
[13] Zagar G., Pejchal V., Mueller M.G., Michelet L., Mortensen A. Fracture toughness measurement in fused quartz using triangular chevron-notched micro-cantilevers. Scripta Mat. 2016; 112: 132-135.

[14] Mueller M.G., Pejchal V., Zagar G., Singh A., Cantoni M., Mortensen A. Fracture toughness testing of nanocrystalline alumina and fused quartz using chevron-notched microbeams. Acta Mat. 2015; 86: 385-395.
[15] Zhang H., Schuster B.E., Wei Q., Ramesh K.T. The design of accurate micro-compression experiments. Scripta Mater. 2006; 54: 181-186.
[16] Hashin Z. Finite thermoelastic fracture criterion with application to laminate cracking analysis. J. Mech. Phys. Solids 44(7), 1996, 1129-1145.
[17] Taylor D. The theory of critical distance. Elsevier, Oxford, 2007.
[18] Leguillon D. Strength or toughness? A criterion for crack onset at a notch, Eur. J. of Mechanics – A/Solids 21, 2002, 61-72.
[19] Weissgraeber P., Leguillon D., Becker W. A review of Finite Fracture Mechanics: crack initiation at singular and non-singular stress raisers. Arch. Appl. Mech. 86, 2016, 375-401.
[20] Parvizi, A., Garrett, K.W., Bailey, J.E. Constrained cracking in glass fibre-reinforced epoxy cross-ply laminates. J. Mater. Sci. 1978; 13: 195–201.
[21] Laschuetza T., Seelig T. Remarks on cohesive dynamic fracture under static pre-stress – with a comparison with finite fracture mechanics. Engng. Fract. Mech. 2021; 242: 107466.
[21] Williams M. L. Stress singularities resulting from various boundary conditions in angular corners of plates in extension. J. Appl. Mech. 1952; 19(4): 526-528.
[22] Leguillon D., Sanchez-Palencia E. Computation of singular solutions in elliptic problems and elasticity, John Wiley & Son New York, and Masson Paris, 1987.
[23] Irwin G. Analysis of stresses and strains near the end of a crack traversing a plate, J. Appl. Mech. 1957; 24: 361–364.
[24] Griffith A. A. VI. The phenomena of rupture and flow in solids. Phil. Trans. of the Royal Society of London. Series A 1921; 221(582-593): 163-198.
[25] Doitrand A., Martin E., Leguillon D. Numerical implementation of the coupled criterion: matched asymptotic and full finite element approaches. Finite Elements in Analysis and Design 2020; 168: 103344.
[26] Elices M., Guinea G.V., Gomez J., Planas J. The cohesive zone model: advantages, limitations and challenges. Engng. Fract. Mech. 69(2), 2002, 137-163.
[27] Francfort G.A., Marigo J.J. Revisiting brittle fracture mechanics as an energy minimization problem. J. Mech. Phys. Solids 1998; 46(8): 1319-1342.
[28] Miehe C., Hofacker M., Welschinger F. A phase-field model for rate independent crack propagation: Robust algorithmic implementation based on operator splits. Comp. Meth. Appl. Mech. Engng. 2010; 199: 2765-2778.
[30] Weißgraeber P., Hell S., Becker W. Crack nucleation in negative geometries. Engng. Fract. Mech. 2016; 168: 93-104.
[31] Sapora A., Cornetti P. Creack onset and propagation stability from a circular hole under biaxial loading. Int. J. Fract. 2018; 214: 97-104.
[29] Hofer A.K., Walton R., Ševeček O., Messing G.L., Bermejo R. Design of damage tolerant and crack-free layered ceramics with textured microstructure. J. Eur. Ceram. Soc. 2020; 40: 427-435.
[30] Leguillon D., Martin E., Lafarie-Frenot M.C. Flexural vs. tensile strength in brittle materials. C.R. Mécanique 2015; 343(4): 275-281.
[31] Doitrand A., Henry R., Meille S. Brittle material strength and fracture toughness estimation from four-point bending test. J. Theor. Comp. Appl. Mech. 2021, 6753.
[32] Weibull W. A statistical distribution function of wide applicability. J. Appl. Mech. 1951; 18(3): 293–297.
[33] Gao H., Ji B., Jäger I.L., Arzt E., Fratzl P. Materials become insensitive to flaws at nanoscale:Lessons from nature. PNAS 2003; 100(10): 5597-6000.

[34] Tada H., Paris P.C., Irwin G.R. The stress analysis of cracks handbook, 2000, 3rd ed., ASME Press, New York.
[35] Henry R., Blay T., Douillard T., Descamps-Mandine A., Zacharie-Aubrun I., Gatt J.M., Langlois C., Meille S. Local fracture toughness measurements in polycrystalline cubic zirconia using micro-cantilever bending tests. Mechanics of Materials 2019; 136: 103086.
[36] Luo W., Kirchlechner C., Fang X., Brinckmann S., Dehm G., Stein F. Influence of composition and crystal structure on the fracture toughness of NbCo2 Laves phase studied by micro-cantilever bending tests. Materials & Design 2018; 145: 116-121.
[37] Pejchal V., Fornabaio M., Žagar G., Mortensen A. The local strength of individual alumina particles. J. Mech. Phys. Solids 2017; 109: 34-49.
[38] Patil S.P., Heider Y., Hernandez Padilla C.A., Cruz-Chu E.R., Markert B. A comparative molecular dynamics-phase-field modeling approach to brittle fracture. Comp. meth. Appl. Mech. Engng. 2016.; 312: 117-129.
[39] Andersons J., Modniks J., Leterrier Y., Tornare G., Dumont P., Manson J. (2008) Evaluation of toughness by finite fracture mechanics from crack onset strain of brittle coatings on polymers. Theor. Appl. Fract. Mech. 2008; 49:151-157.
[40] Leguillon D., martin E. Prediction of multi-cracking in sub-micron films using the coupled criterion. Int. J. Fract. 2018; 209: 187-202.